UNIVERSITY OF AMSTERDAM

UvA-DARE (Digital Academic Repository)

Sporadic radio pulses from a white dwarf binary at the orbital period

de Ruiter, I.; Rajwade, K.M.; Bassa, C.G.; Rowlinson, A.; Wijers, R.A.M.J.; Kilpatrick, C.D.; Stefansson, G.; Callingham, J.R.; Hessels, J.W.T.; Clarke, T.E.; Peters, W.; Wijnands, R.A.D.; Shimwell, T.W.; ter Veen, S.; Morello, V.; Zeimann, G.R.; Mahadevan, S.

DOI
10.1038/s41550-025-02491-0

Publication date
2025

Document Version
Final published version

Published in
Nature Astronomy

License
CC BY

Link to publication

Citation for published version (APA):
de Ruiter, I., Rajwade, K. M., Bassa, C. G., Rowlinson, A., Wijers, R. A. M. J., Kilpatrick, C. D., Stefansson, G., Callingham, J. R., Hessels, J. W. T., Clarke, T. E., Peters, W., Wijnands, R. A. D., Shimwell, T. W., ter Veen, S., Morello, V., Zeimann, G. R., & Mahadevan, S. (2025). Sporadic radio pulses from a white dwarf binary at the orbital period. *Nature Astronomy*, *9*(5), 672-684. https://doi.org/10.1038/s41550-025-02491-0

General rights
It is not permitted to download or to forward/distribute the text or part of it without the consent of the author(s) and/or copyright holder(s), other than for strictly personal, individual use, unless the work is under an open content license (like Creative Commons).

Disclaimer/Complaints regulations
If you believe that digital publication of certain material infringes any of your rights or (privacy) interests, please let the Library know, stating your reasons. In case of a legitimate complaint, the Library will make the material inaccessible and/or remove it from the website. Please Ask the Library: https://uba.uva.nl/en/contact, or a letter to: Library of the University of Amsterdam, Secretariat, P.O. Box 19185, 1000 GD Amsterdam, The Netherlands. You will be contacted as soon as possible.
UvA-DARE is a service provided by the library of the University of Amsterdam (https://dare.uva.nl)

Download date:10 Oct 2026

nature astronomy

Article

https://doi.org/10.1038/s41550-025-02491-0

Sporadic radio pulses from a white dwarf binary at the orbital period

Received: 12 July 2024

Accepted: 28 January 2025

Published online: 12 March 2025

Check for updates

I. de Ruiter[1,2,3] ✉, K. M. Rajwade[4], C. G. Bassa[5], A. Rowlinson[2,5], R. A. M. J. Wijers[2], C. D. Kilpatrick[6], G. Stefansson[2], J. R. Callingham[5,7], J. W. T. Hessels[2,5,8,9], T. E. Clarke[10], W. Peters[10], R. A. D. Wijnands[2], T. W. Shimwell[5,7], S. ter Veen[5], V. Morello[11], G. R. Zeimann[12] & S. Mahadevan[13,14]

Recent observations have revealed rare, previously unknown flashes of cosmic radio waves lasting from milliseconds to minutes, with a periodicity of minutes to an hour. These transient radio signals must originate from sources in the Milky Way and from coherent emission processes in astrophysical plasma. They are theorized to be produced in the extreme and highly magnetized environments around white dwarfs or neutron stars. However, the astrophysical origin of these signals remains contested, and multiple progenitor models may be needed to explain their diverse properties. Here we present the discovery of a transient radio source, ILT J1101 + 5521, whose roughly minute-long pulses arrive with a periodicity of 125.5 min. We find that ILT J1101 + 5521 is an M dwarf–white dwarf binary system with an orbital period that matches the period of the radio pulses, which are observed when the two stars are in conjunction. The binary nature of ILT J1101 + 5521 establishes that some long-period radio transients originate from orbital motion modulating the observed emission, as opposed to an isolated rotating star. We conclude that ILT J1101 + 5521 is probably a polar system where magnetic interaction has synchronized the rotational and orbital periods of the white dwarf. Magnetic interaction and plasma exchange between two stars has been theorized to generate sporadic radio emission, making ILT J1101 + 5521 a potential low-mass analogue to such mechanisms.

ILT J110160.52 + 552119.62 (ILT J1101 + 5521 hereafter) was discovered in a commensal transient search of Low-Frequency Array (LOFAR) all-sky survey data (LOFAR Two-Metre Sky Survey, LoTSS[1]), to detect radio transients on timescales of seconds to hours using radio images[2]. A single bright radio pulse from International LOFAR Telescope (ILT) J1101 + 5521 was detected in data from 8 February 2015, using 8-s snapshot images. We detected six additional pulses in other archival LOFAR data. ILT J1101 + 5521 is localized to a right ascension (RA) (J2000) of 11 h 1 min 50.5 s ± 1.9 s and declination (dec.) (J2000) of +55° 21′ 19.6″ ± 0.39″, equivalently (l, b) = (150.4551° ± 0.0004°, 55.5200° ± 0.0001°) in Galactic coordinates. In total, we discovered seven radio pulses lasting between 30 s and 90 s, with peak flux densities ranging from 41 ± 6 to 256 ± 10 mJy per beam in five LoTSS observations spanning 2015 to 2020, each 8 h in duration. A new 16-h LOFAR monitoring campaign at the end of 2023 yielded no additional detections. A summary of all LOFAR observations and detected pulses is given in Extended Data Table 1.

Figure 1a shows the light curves from the five observations in which we detected radio pulses (Extended Data Table 1 and Extended Data Fig. 1). We use the times of arrival (ToAs) of the pulses to determine a phase-connected timing solution with a period of 125.52978 ± 0.00002 min. Furthermore, we are able to obtain a 3σ

A full list of affiliations appears at the end of the paper. ✉e-mail: iris.deruiter@sydney.edu.au

https://doi.org/10.1038/s41550-025-02491-0

upper limit on the period derivative of 1.711×10^{-11} s s^{-1} (see the Methods for more details and Extended Data Fig. 2 for the timing residuals). Figure 1a shows both the pulses and the non-detections at times when we expect to find pulses based on the periodicity. The pulses have a 2% duty cycle, and the intermittency of the pulses combined with the non-detections in the 2023 follow-up observations (not shown in Fig. 1a) indicates that the source is intrinsically highly variable in nature: we detect a pulse in 7 out of 26 observed periods.

The pulses are visible across the observed range of radio frequencies (120–168 MHz). For the brightest pulse in our sample, we find that the spectral index of the pulse is extraordinarily steep and we determine the spectral index to be $\alpha = -4.1 \pm 1.1$ (Methods), with $S_\nu \propto \nu^\alpha$, where S_ν is the flux density and ν the observing frequency. In addition, for the brightest pulse in our sample, we determine the linear polarization fraction to be $51 \pm 6\%$ for a Faraday rotation measure (RM) of 4.72 ± 0.14 rad m^{-2}. No circularly polarized emission is detected in the pulses, with an upper limit of <1.6% on the circular polarization fraction for the brightest pulse. For the brightest pulse we reprocessed the raw imaging data with a 1-s time resolution (Fig. 1b), which reveals multiple subcomponents in the pulse. Furthermore, the high-time-resolution data allow us to constrain the dispersion measure (DM) to 16 ± 6 pc cm^{-3}.

The Very Large Array (VLA) Low-Band Ionosphere and Transient Experiment (VLITE) archive was also searched for pulses from ILT J1101 + 5521 (Methods and Extended Data Fig. 3), but no additional pulses were found. Simultaneous Swift X-Ray Telescope (XRT) observations were carried out during the 2023 LOFAR observations, yielding an upper limit on the quiescent X-ray luminosity of $L < 1.6 \times 10^{30} \times \left[\frac{d}{504\,\mathrm{pc}}\right]^2$ ergs^{-1} (Methods).

A search in archival multiwavelength datasets on the coordinates of ILT J1101 + 5521 resulted in a match with a star catalogued in the Sloan Digital Sky Survey (SDSS) J110150.52 + 552119.9 (ref. 3), with an *r*-band magnitude $r = 20.86 \pm 0.05$, whose Gaia Data Release 3 (DR3) position[4] is 0.44″ offset from ILT J1101 + 5521, but within the astrometric uncertainty of the radio-derived position of ILT J1101 + 5521 (error in (RA, dec.) = ±(1.9″, 0.39″)). The probability of the optical source aligning with ILT J1101 + 5521 by chance is extremely small (~1 in 10,000; Methods) owing to the low stellar density at high Galactic latitudes. The geometric distance to this star based on Gaia Early Data Release 3 (EDR3) data is 504^{+148}_{-109} pc (ref. 5).

Spectroscopic follow-up (Extended Data Fig. 4) determined the spectral type of the star to be M4.5V and showed that the star has a substantial radial velocity variation of ~200 km s^{-1}. The radial velocity as a function of time is shown in Fig. 2. A simple sinusoid describes the data well, indicating a close-to-circular binary orbit. We fit two sinusoids to the data, one where all fit parameters are unbound and one where we fix the period to the 125.5-min period of the radio pulses, with reduced chi-squared values of 0.62 and 0.79, respectively. There is no significant difference in goodness of fit between the two fits (Bayesian information criterion (BIC) of −107.0 versus BIC of −107.2), clearly showing that the period of the radio pulses is tied to the binary period. Figure 2 also shows the predicted radio pulse arrival time, according to the phase-connected timing solution (see the Methods for a detailed discussion). Assuming a stable orbital period that is equal to the period of the radio pulses, we find that the radio pulses are all emitted when the M dwarf is at superior conjunction with respect to its companion; that is, the M dwarf is seen to be behind and in line with the companion star from the perspective of an observer on Earth. Given the small chance alignment probability, the agreement between the

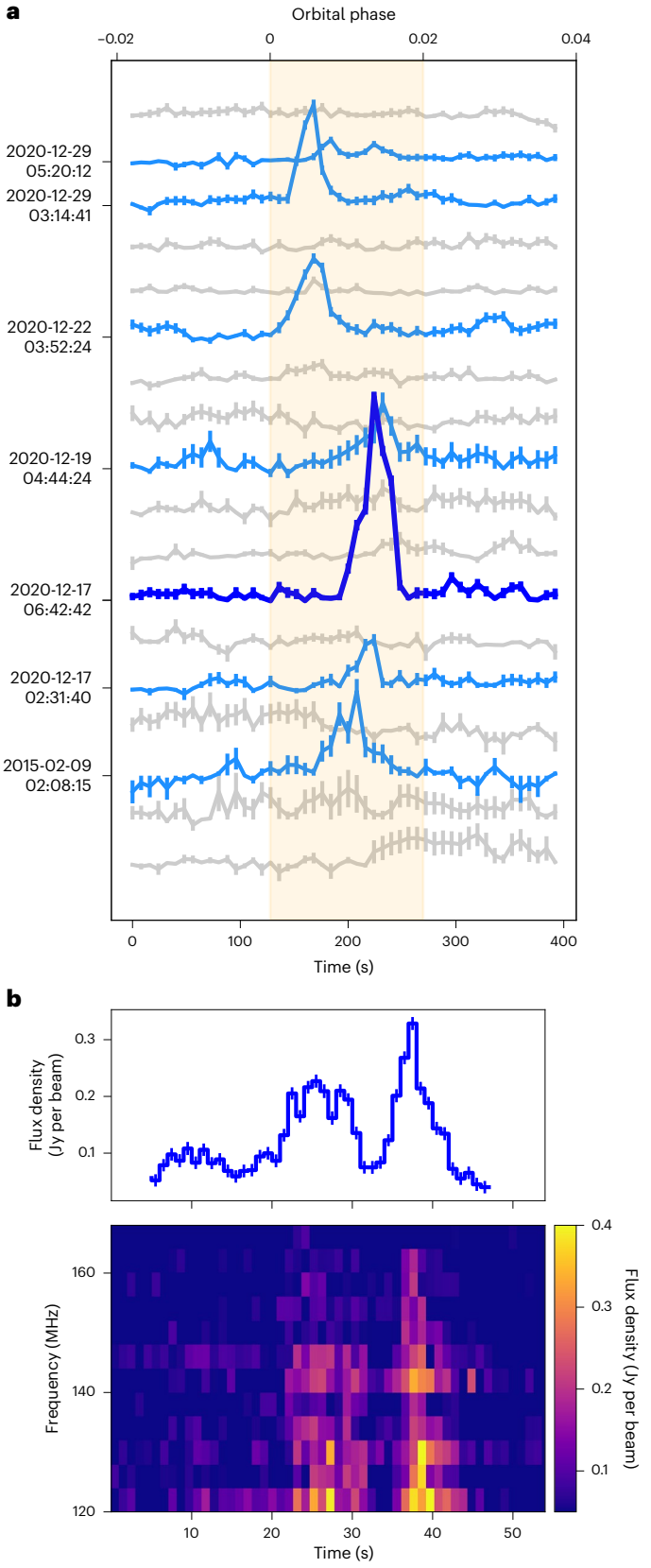

Fig. 1 | Time series of the pulses. a, Light curves (flux density versus time) of the LOFAR-detected pulses (blue) and the non-detections (grey) at times when we expect to find pulses based on their 125.52978-min periodicity. The *y* axis shows the flux density in arbitrary units, and the *x* axis shows time in seconds (bottom) and duty cycle (top). The error bars on the flux indicate 1σ errors. The pulses are aligned according to the measured period, with period derivative assumed to be zero. The orange-shaded region indicates a 2% duty cycle window. The pulses have been observed from 2015 to 2020, and the relative flux scaling between pulses is consistent. **b**, The temporal profile (top) and dynamic spectrum (bottom) of the brightest pulse in our sample, shown in dark blue in **a**. The time resolution is 1 s. Note that this dynamic spectrum is not dedispersed.

https://doi.org/10.1038/s41550-025-02491-0

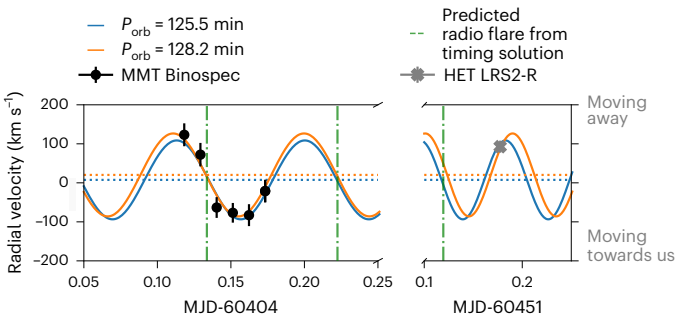

Fig. 2 | Radial velocity of the M dwarf associated with ILT J1101 + 5521. Calculated using MMT-Binospec (black points) and HET LRS2-R (grey point) observations, including 1σ errorbars. The orange line shows the best fit to the data, leaving all parameters free (BIC of −107.0). The blue line shows the best fit to the data if we fix the period to be the 125.5-min period of the radio pulses (BIC of −107.2). The dashed–dotted vertical green lines show the predicted pulse arrival time, according to the phase-connected timing solution. The horizontal dotted lines show the systemic velocities for each fit.

DM of the radio pulses and the distance to the star (Methods), and the periodicity of the radio pulses being equal to the orbital period of this star, we conclude that ILT J1101 + 5521 is a binary system where one of the components is an M4.5V star.

The SDSS ugriz[3] and Pan-STARSS PS1 griz magnitudes[6] yield colour–colour diagrams in which the candidate optical counterpart is consistently offset towards the blue with respect to the main locus of stars, suggesting that the binary companion to the optical star could be a white dwarf. Extended Data Fig. 5 compares ILT J1101 + 5521 with a sample of SDSS objects[3] classified as stars with colour uncertainties <0.1 mag and within 30′ of ILT J1101 + 5521. This figure shows the blue excess, and additionally, it shows that ILT J1101 + 5521 fits the selection criteria used in ref. 7 to select white dwarf–M dwarf binaries.

We note that the blue excess could, in principle, alternatively originate from a star that is highly irradiated by a companion neutron star, as seen in some neutron star–M dwarf binary systems[8]. However, the maximum neutron star (spin-down) luminosity $4\pi^2 I\dot{P}/P^3$, where P is the spin period and assuming $I \approx 10^{45}$ g cm^2, is 1.6×10^{24} erg s^{-1}. This is not sufficient to notably contribute to the u-band luminosity of 5.7×10^{24} erg s^{-1} Å^{-1} ($F_\lambda = 2 \times 10^{18}$ erg cm^{-2} s^{-1} Å^{-1} at 504 pc), after considering the distance between the stars and radiation efficiency. Figure 3 shows a simple least-squares fit to the broadband photometry with a model that allows a main-sequence star only (top) and a model that allows a main-sequence star and a white dwarf (bottom). The difference in BIC for both fits, BIC of 73 and BIC of 57, respectively, is very strong evidence that the latter model, including a main-sequence star and a white dwarf, is preferred. We constrain the M dwarf mass, white dwarf mass, temperature and distance through a Markov-chain Monte-Carlo likelihood analysis[9] (Extended Data Fig. 6). We search for photometric and stochastic variability in the z_i, z_r and z_g photometry from the Zwicky Transient Facility (ZTF[10]), but find no evidence for either (Extended Data Fig. 7). The lack of photometric variability excludes an alternative scenario in which the binary consists of two M dwarfs, and we conclude that the M dwarf companion is a white dwarf.

Using the radial velocity amplitude measurement shown in Fig. 2, we apply the binary mass function to constrain the mass of the white dwarf as a function of orbital inclination, as shown in Fig. 4. The binary mass function is defined as

$$\frac{M_{WD}^3 \sin^3 i}{(M_{MD} + M_{WD})^2} = \frac{P_{orb} K_{MD}^3}{2\pi G}, \quad (1)$$

where M_{WD} is the mass of the white dwarf, M_{MD} is the mass of the M dwarf, i is the inclination of the binary orbit, P_{orb} is the orbital period, K_{MD} is the observed radial velocity of the M dwarf and G is the gravitational constant. Here, we assume a mass of 0.188 $M_\odot$ for the M dwarf (which is a result of the broadband photometry fit, 0.188 ± 0.01 $M_\odot$; Fig. 3), a period of 125.5 min and a radial velocity amplitude of 98 ± 14 km s^{-1}. We find that, even for a white dwarf companion as light as 0.2 $M_\odot$, the inclination of the system has to be smaller than 40°. In the known sample of interacting white dwarf–M dwarf binaries, the white dwarf typically has a mass larger than 0.6 $M_\odot$ (ref. 11). Extended Data Fig. 8 shows that, for white dwarf masses above ~0.25 $M_\odot$, the point of gravitational equipotential between the two stars (Roche–Lobe radius) would equal the stellar radius of the M dwarf.

The radio pulses are incompatible with typical low-frequency stellar radio emission from M dwarfs in terms of luminosity (by five orders of magnitude) and polarimetric properties[12,13] (Methods). Therefore, we conclude that the radio emission originates from the white dwarf or the interaction between the white dwarf and the M dwarf. The high linear polarization fraction indicates the presence of strongly ordered magnetic fields, often found around white dwarfs[14]. White dwarf–M dwarf binaries with highly magnetic white dwarf are the only systems next to neutron stars that are confirmed to emit coherent radio pulses. AR Scorpii[15] and J1912–4410 (ref. 16) are examples of white dwarf binaries that show periodic radio emission, with pulse periods on the order of minutes and orbital periods of about 4 h.

A promising evolutionary model for magnetic white dwarfs in close binary stars is described in detail in ref. 17. The model relies on the late appearance of a high magnetic field, potentially due to a crystallization- and rotation-driven dynamo. A strong white dwarf magnetic field can connect with the field of the M dwarf and provide a synchronizing torque on the white dwarf spin. AR Scorpii and J1912–4410 are thought to be in the beginning stages of the synchronization process. The shorter orbital period of ILT J1101 + 5521 (compared

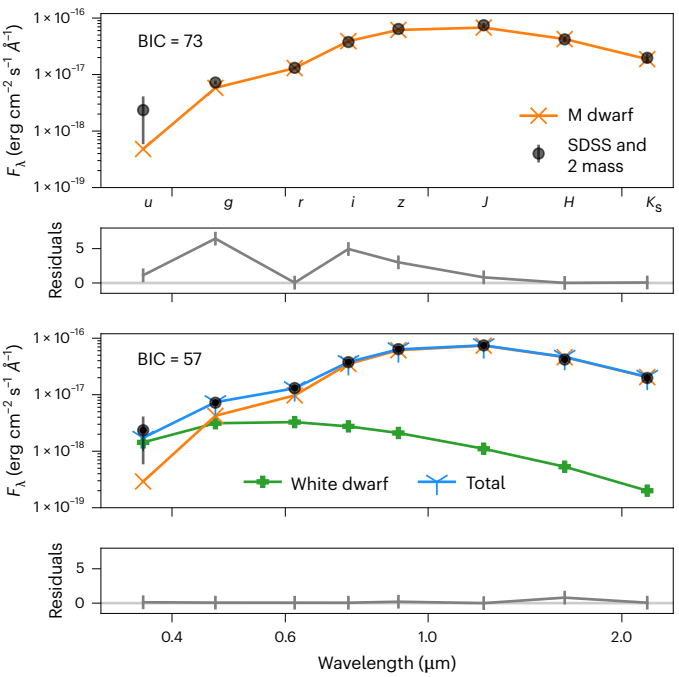

Fig. 3 | Broadband photometry fits for ILT J1101 + 5521. SDSS ugriz and 2MASS JHK$_s$ magnitudes with 1σ errors fit to a single M dwarf model and a combination of an M dwarf and a white dwarf model. Top: an M dwarf with a mass of M = 0.22 $M_\odot$ at a distance of d = 410 pc produces the fit. Bottom: an M dwarf with a a mass of M = 0.18 $M_\odot$ and a white dwarf with a mass of M = 0.63 $M_\odot$ and effective temperature of T_{eff} = 5,156 K at a distance of d = 322 pc produces the fit. The BIC for both fits is shown in the top left of the plot. The residuals are defined as $(O_i - C_i)^2/\sigma_i^2$, where O_i is the observed value, C_i is the model value and σ_i is the error on the observed value. In these normalized residuals, the error bars take a value of 1.

https://doi.org/10.1038/s41550-025-02491-0

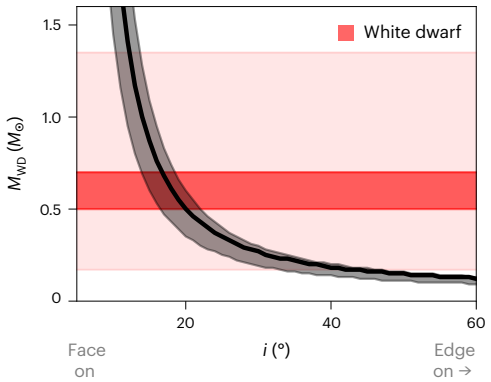

Fig. 4 | Binary mass function showing the white dwarf mass as a function of orbital inclination. The black line shows the allowed companion mass for each inclination (the shaded region around the black line indicates the 1σ error around the mean). A radial velocity amplitude of 98 ± 14 km s^{-1} and an M dwarf mass of 0.188 $M_\odot$ are assumed. In the background we show typical mass ranges of isolated white dwarfs in dark red (0.5–0.7 $M_\odot$ (ref. 106)) and the full range of known white dwarf masses (0.17–1.35 $M_\odot$ (refs. 107,108)) in the lighter shade of red.

with AR Sco and J1912) indicates that the binary system is in the polar stage, where the synchronization process is complete and the M dwarf fills its Roche–Lobe again. This implies that for ILT J1101 + 5521 the white dwarf spin period has synchronized to the orbital period. A more detailed comparison of AR Sco, J1912 and ILT J1101 + 5521 is given in the Methods.

For polars, the magnetic field strength of the white dwarf has increased to over ~10 MG (ref. 18). The formation of an accretion disk is suppressed, but accretion does occur directly onto the magnetic pole of the white dwarf. Polars enter states with little to no accretion, and during these times the system appears as a practically detached white dwarf plus M dwarf system[11,14]. No sustained accretion seems to occur for ILT J1101 + 5521 based on the lack of X-ray emission[19]. Typical X-ray flux in bright accretion phases of polars is around 5×10^{-13} erg cm^{-2} s^{-1} (refs. 20,21), compared with the Swift X-ray upper limit of 5.1×10^{-14} erg cm^{-2} s^{-1} for ILT J1101 + 5521 (Methods). We note that the accretion state of polars changes on timescales of months[21], and the X-ray observations are from December 2023, 3 years after the observed radio pulses.

In addition, the presence of radio pulses indicates little to no accretion, which would probably disturb the creation of coherent radio emission, similar to state-transitioning millisecond pulsar systems (for example, ref. 22). A 125-min period with a M4.5V spectral type donor as observed for ILT J1101 + 5521 sits well within the population of polars (see fig. 7 in ref. 23). Typical polars have a white dwarf mass (~0.6 $M_\odot$) and white dwarf effective temperatures of less than 11,000 K (ref. 11). The temperature of the white dwarf in ILT J1101 + 5521 is likely to be lower ($T_{\rm eff}$ between 4,500 K and 7,500 K; Extended Data Fig. 6), indicating a more evolved system compared with the known sample from optical surveys, which are observationally biased to find hotter systems.

The exact mechanism that produces the radio emission is unknown, but, given the polar configuration, it seems most natural that we observe pulsed radio emission due to beaming effects. Here, we observe the system in a certain geometry (superior conjunction, when the M dwarf is seen to be in line with and behind the white dwarf) once per orbital cycle, effectively looking down a beam of radio emission. In this case, the highly intermittent nature of ILT J1101 + 5521 (pulses are seen in one-quarter of the observed orbits) could be explained by a strong variation in the brightness of the coherent radio emission, similar to what has been proposed for rotating radio transients[24]. The steep spectral index of the brightest radio pulses indicates that the spectrum could be similar to the drastic cut-off seen for electron cyclotron maser instability (ECMI) emission[25]. ECMI emission might explain the radio emission from ILT J1101 + 5521 as magnetic coupling between the M dwarf and white dwarf is confirmed to occur for polar systems[14,17]. Faint circularly polarized minute-duration radio flares have been observed from polar systems at high frequencies[26]. These flares are thought to occur due to ECMI emission caused by the M dwarf moving through the white dwarf magnetosphere. The radio emission from ILT J1101 + 5521 is clearly distinct, as it is observed at much lower frequencies, and the pulses are much brighter and highly linearly polarized. Some of these differences might be explained by invoking a relativistic version of ECMI emission[27].

Although the energy budget is such that the observed radio luminosity could originate from the rotation of the white dwarf (Methods), we argue that the more likely scenario is that the radio emission comes from the interaction of the M dwarf with the white dwarf magnetic field. Alternatively, the radio emission could be triggered by the reconfiguration of the magnetic field (see, for example, refs. 28–32) or, in a more exotic scenario, the radio emission could come from accretion of material onto the magnetic pole of the white dwarf (at very low accretion rates), in a similar fashion to ref. 33 or ref. 34. The high Galactic latitude of ILT J1101 + 5521 makes it easier to study via multiwavelength observations. This will allow us to further study the exact geometry of this binary system, the properties of the two stars and the detailed emission mechanisms at play.

We know of a small population of long-period transient radio sources (periods longer than 10 min)[35–38]. None of the previously detected long-period radio sources has a known binary companion, and the periodicity of the pulses is argued to originate from the spin period of either a neutron star or a white dwarf. ILT J1101 + 5521 is the first long-period radio source that is confirmed to be a binary and the only one with a confirmed white dwarf companion. Furthermore, the radio pulses from ILT J1101 + 5521 have been shown to occur at the orbital period, and at the time of stellar conjunction. We provide a more detailed comparison of ILT J1101 + 5521 with the other long-period radio sources in the Methods. ILT J1101 + 5521 reveals that there are probably multiple progenitors that can produce long-period radio pulses. More speculatively, the existence of ILT J1101 + 5521 may provide an analogy for understanding periodically active fast radio burst sources[39], which could originate from highly magnetized neutron stars interacting with a massive stellar companion[40].

Methods

LOFAR observations and pulse search analysis

The LOFAR[41] is a radio telescope that is composed of many thousands of dipole antennas grouped into stations. The LoTSS[1] aims to image the whole northern sky using 3,168 pointings. The survey has had two major data releases so far: Data Release 1 (DR1)[42] covering 58 pointings and Data Release 2 (DR2)[43] covering 814 pointings, spanning 5,635 deg^2. LoTSS observes between 120 MHz and 168 MHz. The flux densities of detected sources are referenced to a central frequency of 144 MHz.

In ref. 2, a transient detection pipeline is described that looks for transient sources in 8-s to 1-h image snapshots. The transient detection pipeline uses the Live Pulse Finder (LPF)[44]. Transient candidates are marked for further inspection if their position in the snapshot image does not correspond to the position of a known source from the LoTSS catalogue, indicating that the source is visible for only a small part of the full 8-h integration. This transient detection pipeline was tested on a small subset of 58 LoTSS pointings, corresponding to the DR1 fields[2]. For each of these pointings, only the most sensitive part of the primary beam is considered (an inner circular region with a radius of 1.5°).

ILT J1101 + 5521 was detected in the P164+55 pointing in two 8-s snapshots and the 2-min snapshot that encompasses this interval. Reference2 lists all the steps that were undertaken to test whether ILT J1101 + 5521 is a genuine astrophysical source or whether the signal is an imaging artefact. Once ILT J1101 + 5521 was firmly established as an

astrophysical source, additional imaging steps were undertaken to characterize it. This included reimaging the raw visibility data (without subtracting the sky model) with WSCLEAN[45] with increased padding, and deconvolution cycles to obtain snapshot images with the lowest-possible root mean square (RMS) noise. The imaging parameters that were changed from default settings are as follows: the minimum and maximum UV values that are gridded (-minuv-l and -maxuv-l) of 50 and 60,000, respectively, -weight briggs -0.2, -auto-mask 3 and -auto-thresholding 0.3. These parameters are tested in ref. 2 and work well to effectively image point sources. An example of an 8-s image is shown in Supplementary Fig. 1. This is a small cut-out of the full 2.3 × 2.3° image, and shows that the sources are point-like and that there are no imaging artefacts that influence the position and/or flux measurement of ILT J1101 + 5521. In addition, in these new images we use PYSE, a more commonly used source finder that fully captures the properties of point sources in radio images[46]. Extended Data Fig. 1a shows the light curve corresponding to the pulse detected in the 2015 dataset. The two black crosses show the flux density (top) and signal-to-noise ratio (bottom) of the initial detection in the transient detection pipeline (with LPF). It is clear that the improved imaging settings optimize the signal-to-noise ratio of the pulse.

After discovery of this initial pulse, we searched the LOFAR archive for data where the position of ILT J1101 + 5521 lies within the observed field of view. Four additional observations of the P164+55 field were found in the LOFAR Long Term Archive. Again, these observations had an averaged integration time of 8 s, the total observations were 8 h and the direction-independent calibrated data products were readily available. The same methods as in ref. 2 were applied, and six additional pulses were found. Extended Data Fig. 1 shows the flux and signal-to-noise ratio profiles for these pulses. The two pulses identified in the 2020-12-29 dataset are just slightly above the signal-to-noise ratio threshold of 6 used to identify candidate pulses. This signal-to-noise ratio was chosen to perform a slightly deeper search than following the original method with a signal-to-noise ratio of 6.94 (ref. 2). After the reimaging procedure, one of the pulses turned out to be spurious. For all archival data, we reduced the signal-to-noise ratio to 5 to see whether any additional pulses could be identified. The few candidates that we found turned out to disappear after reimaging (similar to the first pulse detected on 19 December 2020; Extended Data Fig. 1, top right). An overview of the observations and detected pulses is shown in Extended Data Table 1. After establishing that we had robustly identified seven bright pulses from this source, we obtained additional LOFAR observations through Director's Discretionary Time (project DDT20_005). Here, we conducted simultaneous beamformed and imaging observations, to obtain both high spatial resolution and subsecond time resolution for any new pulses. Unfortunately, during these observations, no additional pulses were identified. The few candidates that were initially identified after dropping the detection threshold to a signal-to-noise ratio of 5 turned out to disappear after properly reimaging (Extended Data Fig. 1, bottom column).

Periodicity search and timing of the radio pulses

Despite the limited number of radio pulses, we performed a search for any potential underlying periodicity in their arrival times. First we computed the ToA of each pulse. We then barycentred the ToAs before doing any further analysis. Typically, a template is used to compute ToAs, but due to the dearth of pulses to create a stable radio profile for template creation, we decided to use every pulse for the ToA calculation individually by fitting a Gaussian to each pulse to compute the ToA on the basis of the estimated peak of the Gaussian. We note that the uncertainty on the ToA is driven purely by the goodness of fit, which is dependent on the signal-to-noise ratio of each pulse. To get a first estimate of the period, we run the barycentered ToAs through a simple folding algorithm (https://github.com/evanocathain/Useful_RRAT_stuff) that is often used for highly intermittent sources, such as rotating radio transients. For ILT J1101 + 521 we have 7 ToAs, implying 21 unique time differences. Supplementary Fig. 2 shows the number of time differences (between pulse ToAs) that are matched given a certain period, trialling periods from 8 s to 360 min with a timestep $\delta t = 0.01$ s and maximum 2% tolerance in phase to count as a match. This threshold was chosen as it is similar to the phase tolerance identified for GPM J1839−10 (ref. 37) and GLEAM-X J162759.5−523504.3 (ref. 36). We find that a period of 125.52 min, indicated by the red star, lines up all the pulse ToAs to within 2% of a full cycle, and we find that this period is preferred over its harmonics.

In addition, we used ALTRIS (Morello et al., in preparation) (https://github.com/v-morello/altris) a brute-force search algorithm that fits the integer number of rotations within all the gaps between consecutive ToAs. The algorithm attempts to recursively discover the rotation counts under the assumption that a tentative solution for some n shortest gaps is known. Then, a phase model is fitted to the ToA gaps, from which a range of possibilities for the rotation count $n + 1$ is calculated. If no integer rotation counts are possible, the solution is discarded; otherwise, the algorithm attempts to further expand the set of new tentative solutions for the first $n + 1$ gaps. Using this technique, we found the best period of 125.34 min with a Q-factor of 225.6, where the Q-factor is the goodness-of-fit metric for the period ($Q = \frac{1}{\sigma_{\mathrm{ph}}}$, where σ_{ph} is the RMS of the offset of time of the peak of the pulse from the predicted arrival time of the peak). The Q-factor is a measure of the signal-to-noise ratio of the detected period. Hence, one can use this to estimate the uncertainty on the period as $\frac{3}{Q} \times P$ to obtain a 3-σ uncertainty of 1.6 min. We note that, once we use this period as an initial guess for the timing model, the uncertainty on the period is reduced substantialy after the fit to the ToAs as described below. Then, we used TEMPO2 (ref. 47) to fit a simple timing model to the barycentred ToAs. We used only the spin frequency (F0), here also a proxy for the orbital period, as a fitting parameter, keeping the best-known position (RA, dec.) as a fixed parameter. We first phase-connected the six ToAs that were close in time to each other (spanning 10 days) to obtain an RMS of 23.476 s. Projecting that solution back to the first ToA about 4 years before, we obtain a 1σ timing RMS of 26.203 s. Extended Data Fig. 2 shows the timing residuals after subtracting the best-fit timing solution from the ToAs. We note that, if we use the best-fit timing solution obtained from the six ToAs spanning 10 days and extrapolate that to the first ToA 4 years ago, the ToA is offset from the model by only 15–20% of the pulse period. Hence, we infer that, while complete phase connection over the 4 years cannot be guaranteed. The best-fit timing model reasonably predict the ToAs in the future. We provide our best-fit parameters for both timing solutions in Supplementary Table 1. The error quoted in the main text is obtained from the most refined estimate of the period and uncertainty from the timing model as computed by TEMPO2 (ref. 47). The RMS of the residuals can now be used to derive the upper limit on the period derivative. If the timing model does not take into account the period derivative, one would expect a parabolic deviation of the ToA residuals as a function of time. Because we do not see that trend, we assume that the deviation is within the three times the RMS we obtain on the ToA residuals. Thus, the limit on the period derivative

$$\dot{P}_{\mathrm{ul}} = \frac{3\sigma_{\mathrm{ToAs}} \times P}{T^2}, \tag{2}$$

where σ_{ToAs} is the uncertainty-weighted RMS of the timing residuals, P is the spin period and T is the total observing span. This gives us an upper limit of 1.711×10^{-11} s s^{-1} for the period derivative regardless of the origin of the period (spin or orbital origins).

Figure 1a shows the light curves of the LOFAR detections folded with a period of 125.52978 min. The smallest time window that fully captures all pulses implies a duty cycle of ~2%, as well as a jitter in the pulse arrive times of ~1% of the pulse period.

Astrometry of the radio pulses

Based on the five pulses that were identified with peak flux densities of >68 mJy per beam, we perform an astrometric correction on the images to get the most accurate position possible. Using three bright (>200 mJy) point sources close to ILT J1101 + 5521 (within 10′), we define the astrometric offset as the distance between the position of these bright point sources in the snapshot images and their LoTSS catalogue position. Subsequently, we shift ILT J1101 + 5521 in each snapshot according to this systematic offset. The position is then determined again in each snapshot, and the final position is determined by averaging the positions weighted by the signal-to-noise ratio of ILT J1101 + 5521 in the specific snapshot. This yields (RA, dec.) (J2000) = 165.4605° ± 1.9″, 55.35545° ± 0.39″, or RA (J2000) = 11 h 1 m in 50.5 s ± 1.9 s and dec. (J2000) = +55° 21′ 19.6″ ± 0.39″. In addition, we check our procedure by applying FITSWARP[48] to our images. This software is also designed to dedistort ionospheric effects in the image plane. We find a similar correction, that (within errors) matches the result from the aforementioned procedure, but with larger error bars (±10″) on the position.

Pulse polarization and Faraday RM

We estimate the Faraday RM using RM-TOOLS[49] from the Canadian Initiative for Radio Astronomy Data Analysis. For the three brightest pulses, we take the 8-s time slices with the highest total intensity and create full Stokes images with 12 frequency channels. Performing a fit to the Stokes Q and U images, we find RMs of 4.503 ± 0.015 rad m^{-2} for the L801324 pulse, 4.72 ± 0.14 rad m^{-2} for the L801366 pulse and 4.457 ± 0.033 rad m^{-2} for the L801380 pulse. We note that a large polarization position angle swing over the duration of the pulse would distort this result. The apparent variability in RM can be ascribed to the time-variable ionospheric RM contribution, 0.32 ± 0.1, 0.45 ± 0.1 and 0.28 ± 0.1 for the respective pulses. To estimate the RM contribution from the Ionosphere, we used the IONFR software[50] (https://github.com/csobey/ionFR). The code computes the RM expected from the Ionosphere as a function of time for any given day by using the total electron content and the goemagnetic field estimates published by the Global Navigation Satellite System (https://cddis.nasa.gov/). These RMs are consistent with the contribution from the smoothed Galactic foreground[51], precluding the presence of significant local RM contribution from the corona or wind of a star in the system. We find peak linear polarization fractions of 51^{+6}_{-6}% for the L801324 pulse, 13^{+5}_{-3}% for the L801366 pulse and 42^{+7}_{-5}% for the L801380 pulse. No significant circular polarization is detected at the position of ILT J1101 + 5521 in the Stokes V images for any of the pulses in our sample. Performing a forced-flux extraction in the Stokes V images, we find circular polarization fractions of <1.6% for the L801324 pulse, <1.6% for the L801366 pulse and <4.2% for the L801380 pulse. These estimates are limited by the local noise in the Stokes V images.

Dynamic spectrum and DM

The average time resolution of 8 s does not allow a sensitive dispersion analysis. We thus extract the original data products for the observations of the brightest pulse from the LOFAR Long Term Archive (project code LT14_004) and reprocess at the highest-possible time resolution of 1 s. Figure 1b shows the temporal profile and the dynamic spectrum of the reprocessed data for the bright L801324 pulse (Extended Data Table 1). The higher time resolution reveals that the pulse consists of at least two components. The temporal profile was obtained by running the LPF source finder on the 1-s Stokes I images with a signal-to-noise ratio threshold of 3. No clear dispersion track is visible in the dynamic spectrum. We used the LORDS (https://gitlab.com/kmrajwade/lordss) software suite to estimate a DM value of 16 ± 6 pc cm^{-3} (Supplementary Fig. 3). LORDS is an image-plane dedispersion software specifically written to dedisperse transients found in radio imaging surveys (Rajwade et al., in preparation). The Galactic DM in the direction of ILT J1101 + 5521 to a distance of 504 pc (estimated distance to the M dwarf star) is ~10 pc cm^{-3} based on the NE2001 electron density model[52,53]. Within errors, the DM is consistent with the distance to the star. We note that the electron density models in directions well off of the Galactic plane (b = 55.5200° ± 0.0001° for ILT J1101 + 5521) are not constrained as well as directions closer to the Galactic plane.

The best estimate for the spectral index is obtained from the in-band spectrum of the brightest pulse in L801324, as shown in Fig. 1b. The best fit for the first component is $\alpha = -4.5 \pm 1.0$, and $\alpha = -4.8 \pm 1.0$ for the second component, assuming $S \propto \nu^{\alpha}$, where S_{ν} is the flux density and ν is the observing frequency. Averaging over the full pulse, we obtain a very steep spectral index of $\alpha = -4.1 \pm 1.1$. However, we caution that the spectrum is not necessarily well described as a power law.

VLITE observations and analysis

The VLITE (vlite.nrao.edu)[54,55] is a commensal system capable of continuously accessing 64 MHz of bandwidth (centred on 352 MHz) from the 236–492 MHz Low-Band system deployed on the National Radio Astronomy Observatory's Karl G. Jansky Very Large Array. VLITE has been operational since November 2014 recording data from up to 18 antennas during nearly all regular VLA observations. Because VLITE accumulates a large amount of data, an automated calibration and imaging pipeline has been developed[54] that calibrates the visibilities and produces self-calibrated images. The VLITE Database Pipeline[56] then takes these images and creates a source database using the PyBDSF[57] source finding algorithm.

We searched the VLITE Database at the position of ILT J1101 + 5521, but found no catalogued source. We reprocessed all archival VLITE observations within two degrees of ILT J1101 + 5521 where the VLA was in the high-resolution A or B configuration. The images were broken into 60-s snapshots to match the pulse length of ILT J1101 + 5521 and maximize the VLITE sensitivity given the measured steep spectral index. The 225 resulting images were searched by PyBDSF for any source above 5σ and then visually inspected for emission at lower levels for the target position. In the same manner, we searched all 103 VLITE Commensal Sky Survey (VCSS)[58] 28-s snapshot images from six separate days between 2017 and 2023 that cover the source position. Emission was not detected in either the VLITE or VCSS snapshots.

ILT J1101 + 5521 falls between 0.9° and 1.9°, with an average offset of 1.3°, from the correlation centre of the archival VLITE data, resulting in substantial sensitivity loss due to the instrumental response. The VCSS snapshots are observed in highly overlapping, continuous dec. scans across the sky. Similar to the targeted images, the average source position is 1.2° from the VCSS correlation centre, although it ranges from 0.5° to 1.7°. Due to the telescope movement during each of the 28-s VCSS frames, there is a slight additional loss of sensitivity. In Extended Data Fig. 3, we plot the 3σ upper limits from VLITE and VCSS snapshots together with the LOFAR detections and predicted 340-MHz flux on the basis of the measured full pulse spectral index and its uncertainty. Finally, we reimaged the VLITE data between November 2017 and September 2023 with snapshot cadences of 8 s and 2 s to search for signatures of very bright pulses. No emission was detected, and we place 5σ upper limits on bright pulses at 350 and 700 mJy per beam for the 8-s and 2-s cadences, respectively. Archival VLITE and VCSS observations are not sensitive to pulses as steep as measured for the brightest ILT J1101 + 5521 burst ($\alpha = -4.1 \pm 1.1$) as indicated by Extended Data Fig. 3 (bottom). VLITE and VCSS would be sensitive to flatter spectrum or brighter pulses, but unfortunately the temporal coverage in the archive is sparse for this position, making it difficult to rule out such possibilities.

Chance alignment probability with optical counterpart

We performed a cone search through the available optical and near-infrared catalogues using VIZIER[59] around the position of ILT J1101 + 5521. This search yields an optical source at RA (ICRS) of

11 h 1 min 50.5698 s and dec. (ICRS) of +55° 21′ 19.738″, which is 0.44″ offset from ILT J1101 + 5521 but within the astrometric uncertainty of the radio-derived position of ILT J1101 + 5521 (error in (RA, dec.) is ±(1.9″, 0.39″)). To identify the probability of chance association we extract all the sources that lie within a radius of 3° around the position of ILT J1101 + 5521 in Gaia EDR3 (refs. 60,61). We do not apply any other filters to the Gaia catalogue. Subsequently, 10^6 random positions within this patch are drawn and we determine the number of times one of these random positions falls within half an arcsecond of a Gaia source. We find that this happens in only 143 cases and therefore conclude that the probability of chance alignment is $P < 0.00014$. The 3° radius and 10^6 random trial positions were chosen to obtain large samples to increase the robustness of the chance alignment test.

Spectroscopic observations of the M dwarf

We observed the M dwarf associated with ILT J1101 + 5521 using the Binospec optical spectrograph[62] on the 6.5-m Multiple Mirror Telescope (MMT) located at the MMT Observatory on Mt. Hopkins, Arizona. The observation occurred on 4 April 2024 starting at 02:42:49 UTC. We observed the M dwarf with 6 × 900 s exposures, using a 1.0″ long slit and a 270 l mm^{-1} grating, set to a central wavelength of 6,560 Å, and using the LP3800 blocking filter. This resulted in spectral coverage from ~3,900 to 9,300 Å with an average spectral resolution of $R \approx 1{,}530$. Conditions were near photometric at the time of observation, with an average seeing of 1.2″, and the airmass ranged from ~1.1 to 1.3 throughout the observation.

We reduced all observations using pypeit[63], with dome flat and arc lamp calibration files obtained on the same night and instrumental configuration. We used standard pypeit parameters for Binospec, resulting in a signal-to-noise ratio averaged over each optimally extracted spectrum of ~2–3. We then flux calibrated each spectrum with a sensitivity function derived from the standard star G191-B2B obtained in January 2024 and corrected the spectra for telluric absorption using an atmospheric model for the MMT Observatory.

In addition, we observed an optical $R = 2,500$ spectrum of the M dwarf associated with ILT J1101 + 5521 using the LRS2 (ref. 64) instrument on the Hobby–Eberly Telescope[65,66]. We used the LRS2-R unit on the red channel from 6,450 to 8,420 Å. We reduced the LRS2 spectrum using the publicly available Panacea pipeline (https://github.com/grzeimann/Panacea), which performs basic reduction tasks, wavelength calibration, fibre extraction, sky subtraction and flux calibration.

Extended Data Fig. 4 shows the LRS2-R spectrum and a coadded spectrum of the six epochs obtained with Binospec. The absolute flux levels of the ILT J1101 + 5521 optical spectra vary between the two facilities and epochs owing to variations in the sensitivity functions and possible intrinsic variability in the M dwarf (Extended Data Fig. 7 and ref. 67). The highlighted regions in Extended Data Fig. 4 are used for radial velocity fitting below. To determine the spectral type of the M dwarf we fit the obtained spectra to a range of spectral templates, including the ATLAS-T spectra[68] obtained with the Large Sky Area Multi-Object Fiber Spectroscopic Telescope, a suite of Keck LRIS spectra of late-M dwarfs[69], UVES/VLT high-resolution spectra of late type subdwarfs[70] and a complete M spectral type sequence for a sample of confirmed young sources[71] (obtained from http://svo2.cab.inta-csic.es/theory/newov2/index.php). We find that an M4.5V spectrum fits our data best, but we cannot confidently rule out an M4.0V star.

Next, we use the individual epochs to look for a radial velocity signature. In the following, we opt to use the ref. 69 M4.5V model, as the resolution of 1.9 Å is similar to the binned resolution of our observations and the wavelength range overlaps our data. To obtain the Doppler shift of the individual epochs, we select a particular wavelength range. We avoid the noisy edges of the LRS2-R spectrum and disregard data below 8,300 Å and above 8,300 Å (Extended Data Fig. 4). For consistency, we therefore also consider only the spectral range between 6,500 Å and 8,300 Å for the Binospec data. In addition, the signal-to-noise ratio (before binning) is below 3 in each spectral bin for Binospec data below 6,500 Å. Therefore, we cannot be confident that the data are a good representation of the intrinsic spectrum, including potential emission and absorption lines. In this wavelength range, the Binospec data have a resolution of 1.3 Å. We bin the data by a factor of 2 and fit the template to the data while applying a Doppler shift.

For AR Scorpii[15] and J1912−4410 (ref. 16), the radial velocity profile was extracted separately for the Hα emission line (6,562.8 Å). When compared with the absorption lines in the other parts of the spectrum, it was found that the Hα shows a different radial velocity profile. This is because this line probably originates from the irradiated face of the M dwarf and is not expected to show the same amplitude as the star's centre of mass. The difference between the two radial velocity profiles can be used to place constraints on the mass ratio of the system, as shown in refs. 15,16. The Hα line in the individual Binospec spectra does not have a sufficient signal-to-noise ratio to perform a useful radial velocity fit. For the LRS2-R spectrum, however, we determine the Hα centre wavelength to be 6,563.77 ± 0.21 nm. This corresponds to a radial velocity of 44.3 ± 10.3 km s^{-1}, which is notably smaller than the radial velocity obtained from fitting the full spectrum to an absorption line spectrum (92.7 ± 15.5 km s^{-1}). This offset is indicative of the aforementioned scenario, where the Hα emission line originates from the irradiated side of the M dwarf. We leave it to future work to fully probe the Hα radial velocity profile and place further constraints on the mass ratio of the system.

We note that excluding the Hα line from the radial velocity analysis does not affect the outcome in a way that would alter our conclusions. The signal-to-noise ratio in the blue part of the Binospec spectra is insufficient to observe the absorption lines we might expect from the white dwarf (for example, ref. 72).

Swift XRT observations and analysis

To search for any flaring activity of ILT J1101 + 5521, we proposed for Swift observations during the L203* observing runs (Extended Data Table 1). We obtained four individual visits using the XRT[73] in December 2023 for a total time of 13.3 ks on source. We do not find any flares, as no photons are detected at the position of ILT J1101 + 5521. The 3σ upper limit that we find by stacking all observations is a count-rate limit of 1.43×10^{-3} counts s^{-1} (0.3–10 keV). Based on the position of ILT J1101 + 5521, we predict an absorbing Galactic column density of $N_{\rm H} \approx 8.7 \times 10^{19}$ cm^{-2}. This estimate was obtained using the web version of the nH tool[74] in HEASOFT[75]. To convert the count rate upper limit to unabsorbed flux limits, we use WEBPIMMS (https://cxc.harvard.edu/toolkit/pimms.jsp) and assume two spectral models for a pulsar or magnetar, following ref. 76. In the first scenario, we assume thermal emission from a young pulsar, implying a blackbody spectrum with $kT = 0.3$ keV. In the second scenario, we assume non-thermal emission from an energetic pulsar, for which the corresponding spectral scenario is a power law with index $\Gamma = 2$. These two scenarios yield unabsorbed flux limits of 3.3×10^{-14} erg cm^{-2} s^{-1} and 5.1×10^{-14} erg cm^{-2} s^{-1}, respectively. This translates to $L < (1-1.6) \times 10^{30} \times \left[\frac{d}{504\,\mathrm{pc}}\right]^2$ $ergs^{-1}$.

Swift UV/Optical Telescope observations and analysis

During the Swift XRT observations described above, ILT J1101 + 5521 was also simultaneously observed using the Swift UV/Optical Telescope (UVOT[77]). We use several HEASOFT[75] tasks to obtain an upper limit on the UV flux by combining all observations. UVOTSOURCE was used to combine extensions within one visit and extract source and background information, UVOTIMSUM was used to combine the visits and UVOTSOURCE was used to determine the flux upper limit at the ILT J1101 + 5521 position. We use an extraction radius of 15″ on the source location and to determine the background flux. The UVOT flux limit is $<1.0 \times 10^{-17}$ erg s^{-1} cm^{-2} $Å^{-1}$ in the uvm2 filter at 2,246 Å. We note that the data quality of these UVOT observations is low.

All point sources show up as double point sources, which is caused by the attitude control problems of the Swift satellite during the period of early August 2023 until the beginning of April 2024 (due to problems with one of the three on-board gyroscopes; for more details, see refs. 78,79). Unfortunately, all our UVOT data (taken in December 2023) are affected by this issue. We take this into account by increasing our source extraction radius to 15″.

M dwarf colour–colour diagram

Extended Data Fig. 5 compares ILT J1101 + 5521 with a sample of SDSS objects[3] classified as stars with colour uncertainties <0.1 mag and within 30′ of ILT J1101 + 5521. The dashed red line shows the colour–colour selection of white dwarf–main-sequence binaries from ref. 7. Due to selection effects, the vast majority of SDSS white dwarf-main sequence binaries contain a low-mass M-dwarf companion[80]. The selection criteria in ref. 7 should include white dwarfs with effective temperatures ranging from 6,000 to 100,000 K and with surface gravities ranging from 6.5 to 9.5 dex, and secondary star M-dwarf spectral types (M0–M9). The uncertainties on the colours of ILT J1101 + 5521 are large, but Extended Data Fig. 5 indicates a blue excess and shows how ILT J1101 + 5521 could be interpreted as a white dwarf–M dwarf binary.

Broadband photometry fits

To constrain the parameters of a possible binary consisting of a white dwarf and a main-sequence star, we compare the observed ugriz magnitudes from the SDSS Data Release 16 (DR16)[3] and the Two Micron All-Sky Survey (2MASS) JHK_s magnitudes (ref. 81) to absolute magnitude predictions in the same bands from white dwarf cooling models with hydrogen atmospheres (http://www.astro.umontreal.ca/~bergeron/CoolingModels)[82–84] and stellar evolutionary tracks[85–87]. The models are interpolated over the stellar mass, white dwarf mass and white dwarf effective temperature, and the summed flux is corrected for the distance and absorption using an $E_{g-r} = 0.011$ reddening value[88] and $R_V = 3.1$ extinction values[89].

White dwarf parameters via MCMC fitting. Through a Markov-chain Monte-Carlo likelihood analysis[9], the observed magnitudes are well matched for a stellar mass of $M_{MD} = 0.188 \pm 0.010\ M_\odot$ at a distance of $d = 333 \pm 25$ pc (Extended Data Fig. 6). The white dwarf mass and the white dwarf effective temperature range are degenerate, with T_{eff} ranging from 4,500 to 7,500 K for masses of $M_{WD} = 0.2$–$1.3\ M_\odot$. The UVOT upper limit ($<1.0 \times 10^{-17}$ erg s^{-1} cm^{-2} Å^{-1} at 2,246 Å; Methods) is consistent with white dwarfs in this temperature and mass range. The distance following from the Markov-chain Monte-Carlo likelihood analysis is smaller than the Gaia geometric distance of 504^{+148}_{-109} pc, but the distance estimates are consistent within 2σ.

Extended Data Fig. 6 shows the one- and two-dimensional projections of the posterior probability distributions of the parameters used to fit the broadband photometry data presented in Fig. 3. We use flat priors $T_{eff} \in \{3{,}000, 12{,}000\}$ K, $M_{WD} \in \{0.2, 1.3\}\ M_\odot$ and $M_{MS} \in \{0.09, 0.5\}\ M_\odot$ and do not put a prior on the distance. The distance of $d = 333 \pm 25$ pc is offset from the Gaia geometric distance estimate of 504^{+148}_{-109} pc. We try setting a Gaussian prior on the distance ($\mu = 504$ pc and $\sigma = 109$ pc) but find that the model quickly converges to a shorter distance again, with a preferred distance of $d = 337 \pm 25$ pc.

ZTF photometry and analysis

Photometric variability might be expected from a close binary such as ILT J1101 + 5521, either at the orbital period due to irradiation of the M dwarf by the white dwarf[90] or at half the orbital period by ellipsoidal variations from the (close to) Roche–Lobe-filling M dwarf[91]. We analyse the z_i, z_r and z_g photometry from the ZTF[10] for ILT J1101 + 5521. Overall there are 592 data points publicly available in the three filters, where we rejected any points that were obtained in non-optimal conditions (non-zero quality flags) following the recommendations in the ZTF pipeline. This left a total of 451 photometric points with 36 in the z_g filter, 327 in the z_r filter and 88 in the z_i filter, which we used for our analysis. From the ZTF photometry, we find no evidence for modulations at the orbital period or half the orbital period in the periodograms of the ZTF photometry (Extended Data Fig. 7). We note that there are hints of two peaks at 70.3 min and 71.4 min seen in the z_r and z_i bands, respectively (Extended Data Fig. 7, pink cross). However, although these two peaks do not correspond to any peaks in the window functions of the datasets, as the two periods are sufficiently different from each other and correspond to false alarm probabilities around 0.1%, we conclude that the data do not show significant detections of photometric variability.

To probe the sensitivity of the ZTF data to detecting signatures of photometric variability, we performed injection tests where we injected sinusoidal variations with a period of 125.52 min with various amplitudes in the data. Doing so, we place an upper limit of 0.1 mag in the z_r data and 0.05 mag in the z_i data. The expected ellipsoidal variations using the equations in ref. 92 for a white dwarf–M dwarf system are expected to have ellipsoidal variation amplitudes at or below the detectability threshold of the ZTF filters, in agreement with the non-detections in the ZTF filters.

Assuming an M dwarf radius of $R_{MD} = 0.217\ R_\odot$ and an orbital separation of $a = 0.76\ R_\odot$ (for an M dwarf with mass $0.188\ M_\odot$ and a white dwarf with mass $0.6\ M_\odot$), we calculate the maximum inclination angle on the basis of the fact that we do not see eclipses in the ZTF data. We find $i < 74°$. Similarly, we estimate the irradiation luminosity from the white dwarf on the M dwarf. $L_{irr} = L_{WD} \times \frac{\pi R_{MD}^2}{4\pi a^2} = 0.02 L_{WD}$. We thus expect the white dwarf to at most contribute to the luminosity of the M dwarf at a level of ~2%. This is consistent with the ZTF data where we do not find any evidence for photometric variability due to irradiation. Finally, we can rule out an M dwarf–M dwarf binary scenario from the lack of photometric variability in the ZTF data (at twice the orbital period). From the binary mass function, we know that a M4.5V dwarf with a sub-M4.5V dwarf companion ($M < 0.188\ M_\odot$) needs to have an inclination $i > 50°$ to create the observed radial velocity amplitude. However, for short-period double M dwarf binaries with such inclinations, strong photometric variability due to ellipsoidal variations from the (close to) Roche–Lobe-filling M dwarfs is expected and observed[91]. We expect the M dwarf to be close to Roche–Lobe filling for white dwarf masses $M_{WD} > 0.25\ M_\odot$ (Extended Data Fig. 8).

In addition to periodic variability, we test for stochastic variability, following the methods outlined in section 3.2 of ref. 93. We compare the distribution of the number of standard deviations from the mean of the photometric measurements with the maximum expected standard deviation given the number of observations and assume that the measurements follow a Gaussian distribution for a non-variable star. For the green band (36 observations), we find that a maximum deviation of 2.55σ should capture all measurements. There is only one measurement outside this threshold, corresponding to 2.8% of the measurements. In an attempt to consider systematics, we impose a variability threshold of 10% of the measurements being above the expected threshold, that is, we assume that up to 10% of measurements can be adversely affected by systematics. For the other bands, the number of measurements outside the expected threshold is even lower (0.6% for 327 z_r measurements and 2.3% for 88 z_i measurements). We conclude that there is no indication of stochastic variability.

White dwarf spin-down luminosity

Spin-down luminosity is defined as the maximum luminosity that can be derived from the rotation of a magnetized white dwarf or neutron star. We consider whether the radio emission from ILT J1101 + 5521 can be powered by the spin-down of the white dwarf. Assuming that the spin period of the white dwarf has synchronized to the orbital period of the binary (as is the case for polars), we calculate the spin-down luminosity of a pulsar using $L_{spin\text{-}down} = \frac{4\pi^2 I \dot{P}}{P^3}$, where $P = 7{,}531.8$ s and

$\dot{P} \leq 1.7 \times 10^{-11}$. We note that this calculation holds only for a dipolar magnetic field, which is often assumed in the absence of other information[14]. However, individual case studies have shown that the magnetic field topologies of white dwarfs can be highly non-dipolar (see, for example, ref. 94), which will affect the spin-down luminosity. Assuming $I \approx 10^{50}$ g cm^2 for a typical white dwarf, we find that $L_{\text{spin-down}} < 1.6 \times 10^{29}$ erg s^{-1}. The peak radio luminosity (256 mJy at 144 MHz) is $L_{\nu,\text{rad}} = 7.8 \times 10^{19} \left[\frac{d}{504\,\text{pc}}\right]^2$ erg s^{-1}Hz^{-1}. Integrating over the LOFAR bandwidth of 48 MHz and assuming a flat spectrum over this bandwidth, we find $L_{\text{rad}} = 3.7 \times 10^{27} \left[\frac{d}{504\,\text{pc}}\right]^2$ ergs^{-1}. This implies that, for a radio efficiency of $\xi \approx 10^{-2}$, the spin-down luminosity could power the observed radio emission. For neutron stars, radio efficiencies up to 10^{-2} have been observed[95], but typical radio efficiencies for pulsars are much lower ($<10^{-2}$). We cannot confidently exclude a white dwarf spin-down origin for the radio emission, but extremely high radio efficiencies are required, making this an unlikely scenario.

Chromospheric activity from the M dwarf

We use the X-ray observations to investigate whether the M dwarf is chromospherically active. Usually, the X-ray luminosity of chromospherically active M dwarfs in the range of 0.2–2 keV varies between 2×10^{26} and 3.6×10^{29} erg s^{-1} (see supplementary material in ref. 13). For ILT J1101 + 5521, assuming a soft X-ray upper limit of ~1×10^{-14} erg cm^{-2} s^{-1} and a distance of 504 pc, this translates to $L < 3 \times 10^{29}$ erg s^{-1}. Based on the X-ray limits, we cannot exclude chromospheric activity. Another indicator for chromospheric activity is the chromospheric emission lines Hα and Ca II, which are the result of magnetic heating of the stellar atmosphere. The spectra obtained in this work show a clear Hα emission line (Extended Data Fig. 4). This emission line follows the same radial velocity pattern as the M dwarf; thus, the Hα line originates from the M dwarf. Following ref. 96, we estimate the equivalent width (EW) of the Hα emission line in the HET LRS2-R spectrum, as the signal-to-noise ratio and spectral resolution are higher than for the combined MMT spectrum. We find the EW of Hα to be −9.1, clearly indicating strong chromospheric activity when compared with the sample of ref. 96 (see their fig. 2).

Radio emission from the M dwarf

Coherent radio emission from stellar systems can be produced by two mechanisms: plasma emission that occurs at the ambient plasma frequency and its harmonics, and cyclotron emission that occurs at the ambient cyclotron frequency and its harmonics[97]. Both plasma and cyclotron emission are expected to be highly circularly polarized[98].

We therefore conclude that ILT J1101 + 5521 cannot originate from the M dwarf, as the circular polarization fraction of the radio pulses is less than a few per cent at most. In ref. 13, it was found that even the weakest circularly polarized M dwarf still showed a circular polarization fraction of 38%. Furthermore, the brightest radio luminosity (assuming the distance to the star to be 504 pc) is roughly $L = 7.8 \times 10^{19}$ erg s^{-1} Hz^{-1}, which is five orders of magnitude brighter than the population of M dwarfs that has been observed at low radio frequencies[13]. Stellar flares with moderate linear polarization fractions have been observed[12,99,100], but these sources were always highly circularly polarized as well. We do not know of any physical mechanism by which the M dwarf could produce the observed radio emission. Therefore, this radio emission must originate from the interaction between the companion and the M dwarf.

Chromospherically active binaries

Close stellar binaries, such as RS Canum Venaticorum (RS CVn) variables, are the most luminous stellar radio systems and show heightened levels of chromospheric activities. The typical X-ray luminosity of chromospherically active binaries is >10^{30} erg s^{-1} (refs. 101–103). However, RS CVn systems with X-ray luminosities as low as 10^{29} erg s^{-1} have also been found[102]. For ILT J1101 + 5521, the X-ray limit is $L < (1\text{-}1.6) \times 10^{30} \times \left[\frac{d}{504\,\text{pc}}\right]^2$ ergs^{-1}. A stronger argument against a RS CVn origin for ILT J1101 + 5521 is the relation between the X-ray and radio luminosity of such systems, the Güdel–Benz relation $L_X = 9.48 \times 10^{18} L_{\nu,rad}^{0.73}$ (ref. 104). For the radio luminosities of the detected pulses ($L_{\nu,\text{rad}} = 1.4\text{-}7.8 \times 10^{19} \left[\frac{d}{504\,\text{pc}}\right]^2$ erg s^{-1}Hz^{-1}), this implies X-ray luminosities of $L_X = 0.9\text{–}3.2 \times 10^{33}$ erg s^{-1}, which is three orders of magnitude above our X-ray upper limit. Deviations from the Güdel–Benz relation have been observed[102], but no systems with over an order-of-magnitude discrepancy between X-ray and radio luminosities have been found. Moreover, the radio emission from RS CVn systems is thought to be produced by the ECMI, which is expected to yield a circularly polarized radio signature[98,101]. Finally, the RV signature and optical photometry imply a mass that is consistent with a compact object—not with a similar mass object. Therefore, we conclude that ILT J1101 + 5521 is not a close chromospherically active stellar binary.

Comparison with AR Scorpii, J1912−4410 and other long-period transients

A detailed comparison of ILT J1101 + 5521 with AR Scorpii[15], J1912−4410 (ref. 16) and other long-period transient radio sources[35–38] is provided in the Supplementary Information.

Data availability

The data that support the findings of this study are available via Zenodo at https://doi.org/10.5281/zenodo.14238890 (ref. 105).

Code availability

The timing was modelled using TEMPO2 (ref. 47). The specific Python scripts used in the data analysis are available via Zenodo at https://doi.org/10.5281/zenodo.14238890 (ref. 105).

References

1. Shimwell, T. et al. The LOFAR Two-Metre Sky Survey-I. Survey description and preliminary data release. *Astron. Astrophys.* **598**, 104 (2017).
2. Ruiter, I. et al. Transient study using LOTSS-framework development and preliminary results. *Mon. Not. R. Astron. Soc.* **531**, 4805–4822 (2024).
3. Ahumada, R. et al. The 16th data release of the Sloan Digital Sky Surveys: first release from the APOGEE-2 southern survey and full release of eBOSS spectra. *Astrophys. J. Suppl. Ser.* **249**, 3 (2020).
4. Vallenari, A. et al. Gaia data release 3-summary of the content and survey properties. *Astron. Astrophys.* **674**, 1 (2023).
5. Bailer-Jones, C. A. L., Rybizki, J., Fouesneau, M., Demleitner, M. & Andrae, R. Estimating distances from parallaxes. V. Geometric and photogeometric distances to 1.47 billion stars in Gaia Early Data Release 3. *Astron. J.* **161**, 147 (2021).
6. Chambers, K. C. et al. The Pan-STARRS1 surveys. Preprint at https://arxiv.org/abs/1612.05560 (2016).
7. Rebassa-Mansergas, A. et al. The SDSS spectroscopic catalogue of white dwarf-main-sequence binaries: new identifications from DR 9–12. *Mon. Not. R. Astron. Soc.* **458**, 3808–3819 (2016).
8. Wadiasingh, Z., Venter, C., Harding, A. K., Böttcher, M. & Kilian, P. Pressure balance and intrabinary shock stability in rotation-powered-state redback and transitional millisecond pulsar binary systems. *Astrophys. J.* **869**, 120 (2018).
9. Foreman-Mackey, D., Hogg, D. W., Lang, D. & Goodman, J. emcee: the MCMC hammer. *Publ. Astron. Soc. Pac.* **125**, 306 (2013).
10. Masci, F. J. et al. The Zwicky Transient Facility: data processing, products, and archive. *Publ. Astron. Soc. Pac.* **131**, 018003 (2018).

11. Townsley, D. M. & Gänsicke, B. T. Cataclysmic variable primary effective temperatures: constraints on binary angular momentum loss. *Astrophys. J.* **693**, 1007 (2009).
12. Callingham, J. et al. Low-frequency monitoring of flare star binary CR Draconis: long-term electron-cyclotron maser emission. *Astron. Astrophys.* **648**, 13 (2021).
13. Callingham, J. et al. The population of M dwarfs observed at low radio frequencies. *Nat. Astron.* **5**, 1233–1239 (2021).
14. Ferrario, L., Martino, D. & Gänsicke, B. T. Magnetic white dwarfs. *Space Sci. Rev.* **191**, 111–169 (2015).
15. Marsh, T. et al. A radio-pulsing white dwarf binary star. *Nature* **537**, 374–377 (2016).
16. Pelisoli, I. et al. A 5.3-min-period pulsing white dwarf in a binary detected from radio to X-rays. *Nat. Astron.* **7**, 931–942 (2023).
17. Schreiber, M. R., Belloni, D., Gänsicke, B. T., Parsons, S. G. & Zorotovic, M. The origin and evolution of magnetic white dwarfs in close binary stars. *Nat. Astron.* **5**, 648–654 (2021).
18. Ramsay, G., Wheatley, P. J., Norton, A. J., Hakala, P. & Baskill, D. The defining characteristics of intermediate polars–the case of three-candidate systems. *Mon. Not. R. Astron. Soc.* **387**, 1157–1162 (2008).
19. King, A. & Watson, M. Mass transfer rates and the soft X-ray excess in am herculis binaries. *Mon. Not. R. Astron. Soc.* **227**, 205–211 (1987).
20. Belle, K. E., Howell, S. B. & Mills, A. Euve observations of the magnetic cataclysmic variable qq vulpeculae. *Publ. Astron. Soc. Pac.* **112**, 343 (2000).
21. Worpel, H. et al. X-ray and optical observations of four polars. *Astron. Astrophys.* **592**, 114 (2016).
22. Stappers, B. et al. A state change in the missing link binary pulsar system PSR J1023 + 0038. *Astrophys. J.* **790**, 39 (2014).
23. Knigge, C. The donor stars of cataclysmic variables. *Mon. Not. R. Astron. Soc.* **373**, 484–502 (2006).
24. Yuen, R. Simulating radio-off fractions in rotating radio transients. *Astron. Astrophys.* **683**, 108 (2024).
25. Zarka, P. Auroral radio emissions at the outer planets: observations and theories. *J. Geophys. Res. Planets* **103**, 20159–20194 (1998).
26. Barrett, P., Dieck, C., Beasley, A. J., Mason, P. A. & Singh, K. P. Radio observations of magnetic cataclysmic variables. *Adv. Space Res.* **66**, 1226–1234 (2020).
27. Qu, Y. & Zhang, B. Magnetic interaction in white dwarf binaries as mechanism for long-period radio transients. Preprint at https://arxiv.org/abs/2409.05978 (2024).
28. Zhang, B. Fast radio bursts from interacting binary neutron star systems. *Astrophys. J. Lett.* **890**, 24 (2020).
29. Most, E. R. & Philippov, A. A. Reconnection-powered fast radio transients from coalescing neutron star binaries. *Phys. Rev. Lett.* **130**, 245201 (2023).
30. Lyubarsky, Y. Fast radio bursts from reconnection in a magnetar magnetosphere. *Astrophys. J.* **897**, 1 (2020).
31. Cooper, A. et al. Pulsar revival in neutron star mergers: multimessenger prospects for the discovery of pre-merger coherent radio emission. *Mon. Not. R. Astron. Soc.* **519**, 3923–3946 (2023).
32. Lyutikov, M. Electrodynamics of binary neutron star mergers. *Mon. Not. R. Astron. Soc.* **483**, 2766–2777 (2019).
33. Katz, J. FRB as products of accretion disc funnels. *Mon. Not. R. Astron. Soc.: Letters* **471**, 92–95 (2017).
34. Gu, W.-M., Dong, Y.-Z., Liu, T., Ma, R. & Wang, J. A neutron star–white dwarf binary model for repeating fast radio burst 121102. *Astrophys. J. Lett.* **823**, 28 (2016).
35. Hyman, S. D. et al. A powerful bursting radio source towards the Galactic Centre. *Nature* **434**, 50–52 (2005).
36. Hurley-Walker, N. et al. A radio transient with unusually slow periodic emission. *Nature* **601**, 526–530 (2022).
37. Hurley-Walker, N. et al. A long-period radio transient active for three decades. *Nature* **619**, 487–490 (2023).
38. Caleb, M. et al. An emission-state-switching radio transient with a 54-minute period. *Nat. Astron.* **8**, 1159–1168 (2024).
39. Amiri, M. et al. Periodic activity from a fast radio burst source. *Nature* **582**, 351–355 (2020).
40. Tendulkar, S. P. et al. The 60 pc environment of FRB 20180916b. *Astrophys. J. Lett.* **908**, 12 (2021).
41. Haarlem, M. P. et al. LOFAR: the low-frequency array. *Astron. Astrophys.* **556**, 2 (2013).
42. Shimwell, T. et al. The LOFAR Two-Metre Sky Survey-II. First data release. *Astron. Astrophys.* **622**, 1 (2019).
43. Shimwell, T. et al. The LOFAR Two-Metre Sky Survey-V. Second data release. *Astron. Astrophys.* **659**, 1 (2022).
44. Ruhe, D. et al. Detecting dispersed radio transients in real time using convolutional neural networks. *Astron. Comput.* **38**, 100512 (2022).
45. Offringa, A. et al. WSClean: an implementation of a fast, generic wide-field imager for radio astronomy. *Mon. Not. R. Astron. Soc.* **444**, 606–619 (2014).
46. Carbone, D. et al. PySE: software for extracting sources from radio images. *Astron. Comput.* **23**, 92–102 (2018).
47. Hobbs, G., Edwards, R. & Manchester, R. TEMPO2, a new pulsar-timing package—I. An overview. *Mon. Not. R. Astron. Soc.* **369**, 655–672 (2006).
48. Hurley-Walker, N. & Hancock, P. J. De-distorting ionospheric effects in the image plane. *Astron. Comput.* **25**, 94–102 (2018).
49. Purcell, C. R., Van Eck, C. L., West, J., Sun, X. H. & Gaensler, B. M. RM-Tools: rotation measure (RM) synthesis and stokes QU-fitting. *Astrophysics Source Code Library* 2005.003 (2020).
50. Sotomayor-Beltran, C. et al. Calibrating high-precision Faraday rotation measurements for LOFAR and the next generation of low-frequency radio telescopes. *Astron. Astrophys.* **552**, 58 (2013).
51. O'Sullivan, S. et al. The Faraday rotation measure grid of the LOFAR Two-Metre Sky Survey: data release 2. *Mon. Not. R. Astron. Soc.* **519**, 5723–5742 (2023).
52. Cordes, J. M. & Lazio, T. J. W. NE2001. I. A new model for the Galactic distribution of free electrons and its fluctuations. Preprint at https://doi.org/10.48550/arXiv.astro-ph/0207156 (2002).
53. Cordes, J. in *Milky Way Surveys: The Structure and Evolution of Our Galaxy* vol. 317 (eds Clemens, D., Shah, R. Y. & Brainerd, T.) 211–217 (Astronomical Society of the Pacific, 2004).
54. Polisensky, E. et al. Exploring the transient radio sky with vlite: early results. *Astrophys. J.* **832**, 60 (2016).
55. Clarke, T. E. et al. in *Ground-Based and Airborne Telescopes VI* vol. 9906 (eds Hall, H. J., Gilmozzi, R. & Marshall, H. K.) 99065 (SPIE, 2016).
56. Polisensky, E., Richards, E., Clarke, T., Peters, W. & Kassim, N. Astronomical Data Analysis Software and Systems XXVIII. In *Astronomical Society of the Pacific Conference Series* vol. 523 (eds Teuben, P. J., Pound, M. W., Thomas, B. A. & Warner, E. M.) 441–445 (Astronomical Society of the Pacific, 2019).
57. Mohan, N. & Rafferty, D. *PyBDSF: Python Blob Detection and Source Finder* record ascl:1502.007 (Astrophysics Source Code Library, 2015).
58. Peters, W., Clarke, T., Giacintucci, S., Nyland, K. & Polisensky, E. *The VLITE Commensal Sky Survey (VCSS) Epoch 1 Bright Catalogue Release* (CIRADA, 2023).
59. Ochsenbein, F., Bauer, P. & Marcout, J. The Vizier database of astronomical catalogues. *Astron. Astrophys. Suppl.* **143**, 23–32 (2000).

60. Prusti, T. et al. The Gaia mission. *Astron. Astrophys.* **595**, 1 (2016).
61. Brown, A. G. et al. Gaia early data release 3-summary of the contents and survey properties. *Astron. Astrophys.* **649**, 1 (2021).
62. Fabricant, D. et al. Binospec: a wide-field imaging spectrograph for the mmt. *Publ. Astron. Soc. Pac.* **131**, 075004 (2019).
63. Prochaska, J. et al. PypeIt: the Python spectroscopic data reduction pipeline. *J. Open Source Softw.* **5**, 2308 (2020).
64. Chonis, T. S. et al. in *Ground-Based and Airborne Instrumentation for Astronomy VI* vol. 9908 (eds Evans, C. J., Simard, L. & Takami, H.) 1345–1372 (SPIE, 2016).
65. Ramsey, L. W. et al. in *Advanced Technology Optical/IR Telescopes VI* vol. 3352 (ed. Stepp, L. M.) 34–42 (SPIE, 1998).
66. Hill, G. J. et al. The HETDEX instrumentation: Hobby–Eberly telescope wide-field upgrade and virus. *Astron. J.* **162**, 298 (2021).
67. Mignon, L. et al. Characterisation of stellar activity of M dwarfs-I. Long-timescale variability in a large sample and detection of new cycles. *Astron. Astrophys.* **675**, 168 (2023).
68. Ji, W. et al. All spectral type lamost spectra library (atlas). *Astrophys. J. Suppl. Ser.* **265**, 61 (2023).
69. Kirkpatrick, J. D., Henry, T. J. & McCarthy Jr, D. W. A standard stellar spectral sequence in the red/near-infrared-classes K5 to M9. *Astrophys. J. Suppl. Ser.* **77**, 417–440 (1991).
70. Rajpurohit, A. et al. High-resolution spectroscopic atlas of M subdwarfs. Effective temperature and metallicity. *Astron. Astrophys.* **564**, 90 (2014).
71. Bayo, A. et al. Spectroscopy of very low mass stars and brown dwarfs in the Lambda Orionis star forming region-I. Enlarging the census down to the planetary mass domain in Collinder 69. *Astron. Astrophys.* **536**, 63 (2011).
72. Pyrzas, S. et al. Post-common envelope binaries from SDSS–XV. Accurate stellar parameters for a cool 0.4 $M_{\odot}$ white dwarf and a 0.16 $M_{\odot}$ M dwarf in a 3 h eclipsing binary. *Mon. Not. R. Astron. Soc.* **419**, 817–826 (2012).
73. Burrows, D. N. et al. The Swift X-Ray Telescope. *Space Sci. Rev.* **120**, 165–195 (2005).
74. Bekhti, N. B. et al. HI4PI: a full-sky H i survey based on EBHIS and GASS. *Astron. Astrophys.* **594**, 116 (2016).
75. *HEAsoft: Unified Release of FTOOLS and XANADU* (NASA High Energy Astrophysics Science Archive Research Center, 2014).
76. Rea, N. et al. Constraining the nature of the 18 min periodic radio transient GLEAM-X J162759.5-523504.3 via multiwavelength observations and magneto-thermal simulations. *Astrophys. J.* **940**, 72 (2022).
77. Roming, P. W. et al. The Swift ultra-violet/optical telescope. *Space Sci. Rev.* **120**, 95–142 (2005).
78. Cenko, B. Swift attitude control affecting some UVOT images. *GRB Coord. Netw.* **34633**, 1 (2023).
79. Cenko, B. Swift satellite resumes pointed science observations. *GRB Coord. Netw.* **36033**, 1 (2024).
80. Rebassa-Mansergas, A., Gänsicke, B., Schreiber, M. R., Koester, D. & Rodríguez-Gil, P. Post-common envelope binaries from SDSS–VII. A catalogue of white dwarf-main sequence binaries. *Mon. Not. R. Astron. Soc.* **402**, 620–640 (2010).
81. Skrutskie, M. et al. The Two Micron All Sky Survey (2MASS). *Astron. J.* **131**, 1163 (2006).
82. Holberg, J. & Bergeron, P. Calibration of synthetic photometry using da white dwarfs. *Astron. J.* **132**, 1221 (2006).
83. Bédard, A., Bergeron, P., Brassard, P. & Fontaine, G. On the spectral evolution of hot white dwarf stars. I. A detailed model atmosphere analysis of hot white dwarfs from SDSS DR12. *Astrophys. J.* **901**, 93 (2020).
84. Blouin, S., Dufour, P. & Allard, N. F. A new generation of cool white dwarf atmosphere models. I. Theoretical framework and applications to DZ stars. *Astrophys. J.* **863**, 184 (2018).
85. Bressan, A. et al. Parsec: stellar tracks and isochrones with the padova and trieste stellar evolution code. *Mon. Not. R. Astron. Soc.* **427**, 127–145 (2012).
86. Chen, Y. et al. Improving parsec models for very low mass stars. *Mon. Not. R. Astron. Soc.* **444**, 2525–2543 (2014).
87. Chen, Y. et al. Parsec evolutionary tracks of massive stars up to 350 $M_{\odot}$ at metallicities $0.0001 \leq z \leq 0.04$. *Mon. Not. R. Astron. Soc.* **452**, 1068–1080 (2015).
88. Green, G. M., Schlafly, E., Zucker, C., Speagle, J. S. & Finkbeiner, D. A 3D dust map based on Gaia, Pan-STARRS 1, and 2MASS. *Astrophys. J.* **887**, 93 (2019).
89. Schlafly, E. F. & Finkbeiner, D. P. Measuring reddening with Sloan Digital Sky Survey stellar spectra and recalibrating SFD. *Astrophys. J.* **737**, 103 (2011).
90. Parsons, S. et al. The shortest period detached white dwarf + main-sequence binary. *Mon. Not. R. Astron. Soc.* **419**, 304–313 (2012).
91. Drake, A. et al. Ultra-short period binaries from the Catalina surveys. *Astrophys. J.* **790**, 157 (2014).
92. Gai, A. D. & Knuth, K. H. Bayesian model testing of ellipsoidal variations on stars due to hot Jupiters. *Astrophys. J.* **853**, 49 (2018).
93. Pelisoli, I. et al. A survey for radio emission from white dwarfs in the VLA Sky Survey. *Mon. Not. R. Astron. Soc.* **531**, 1805–1822 (2024).
94. Euchner, F., Reinsch, K., Jordan, S., Beuermann, K. & Gänsicke, B. T. Zeeman tomography of magnetic white dwarfs-II. The quadrupole-dominated magnetic field of HE 1045-0908. *Astron. Astrophys.* **442**, 651–660 (2005).
95. Szary, A., Zhang, B., Melikidze, G. I., Gil, J. & Xu, R.-X. Radio efficiency of pulsars. *Astrophys. J.* **784**, 59 (2014).
96. Newton, E. R. et al. The Hα emission of nearby M dwarfs and its relation to stellar rotation. *Astrophys. J.* **834**, 85 (2017).
97. Melrose, D. & Dulk, G. A. Electron-cyclotron masers as the source of certain solar and stellar radio bursts. *Astrophys. J.* **259**, 844–858 (1982).
98. Dulk, G. A. Radio emission from the sun and stars. *Annu. Rev. Astron. Astrophys.* **23**, 169–224 (1985).
99. Lynch, C., Lenc, E., Kaplan, D., Murphy, T. & Anderson, G. 154 Mhz detection of faint, polarized flares from UV Ceti. *Astrophys. J. Lett.* **836**, 30 (2017).
100. Zic, A. et al. ASKAP detection of periodic and elliptically polarized radio pulses from UV Ceti. *Mon. Not. R. Astron. Soc.* **488**, 559–571 (2019).
101. Toet, S. et al. Coherent radio emission from a population of RS Canum Venaticorum systems. *Astron. Astrophys.* **654**, 21 (2021).
102. Vedantham, H. et al. Peculiar radio–X-ray relationship in active stars. *Astrophys. J. Lett.* **926**, 30 (2022).
103. Callingham, J. et al. V-LOTSS: the circularly polarised LOFAR Two-Metre Sky Survey. *Astron. Astrophys.* **670**, 124 (2023).
104. Williams, P. K. G., Cook, B. A. & Berger, E. Trends in ultracool dwarf magnetism. I. X-ray suppression and radio enhancement. *Astrophys. J.* **785**, 9 (2014).
105. de Ruiter, I. et al. Reproduction package for 'Sporadic radio pulses from a white dwarf binary at the orbital period'. *Zenodo* https://doi.org/10.5281/zenodo.14238890 (2025).
106. Kepler, S. O. et al. White dwarf mass distribution in the SDSS. *Mon. Not. R. Astron. Soc.* **375**, 1315–1324 (2007).
107. Hermes, J. et al. SDSS J184037.78+642312.3: the first pulsating extremely low mass white dwarf. *Astrophys. J. Lett.* **750**, 28 (2012).
108. Caiazzo, I. et al. A highly magnetized and rapidly rotating white dwarf as small as the moon. *Nature* **595**, 39–42 (2021).
109. Foreman-Mackey, D. corner.py: scatterplot matrices in Python. *J. Open Source Softw.* **1**, 24 (2016).

110. Zechmeister, M. et al. The CARMENES search for exoplanets around M dwarfs—two temperate Earth-mass planet candidates around Teegarden's Star. *Astron. Astrophys.* **627**, 49 (2019).
111. Eggleton, P. P. Approximations to the radii of Roche lobes. *Astrophys. J.* **268**, 368 (1983).

Acknowledgements

We appreciate the input from S. Toonen's research group at the Anton Pannekoek Institute for Astronomy and thank M. Caleb, N. Hurley-Walker, S. McSweeney and Z. Wadiasingh for their suggestions and discussions. This Article is based in part on data obtained with the International LOFAR Telescope (ILT) under project codes LC3_008, LT14_003 and DDT20_005. LOFAR[41] is designed and constructed by ASTRON. It has observing, data processing and data storage facilities in several countries that are owned by various parties (each with their own funding sources) and that are collectively operated by the ILT foundation under a joint scientific policy. The ILT resources have benefitted from the following recent major funding sources: CNRS-INSU, Observatoire de Paris and Université d'Orléans, France; BMBF, MIWF-NRW, MPG, Germany; Science Foundation Ireland (SFI), Department of Business, Enterprise and Innovation (DBEI), Ireland; NWO, the Netherlands; The Science and Technology Facilities Council, UK; Ministry of Science and Higher Education, Poland. This work made use of data supplied by the UK Swift Science Data Centre at the University of Leicester. This research has made use of the VizieR catalogue access tool, CDS, Strasbourg, France 10.26093/CDS/VIZIER. The original description of the VizieR service was published in ref. 59. This work has made use of data from the European Space Agency (ESA) mission Gaia (https://www.cosmos.esa.int/gaia), processed by the Gaia Data Processing and Analysis Consortium (DPAC, https://www.cosmos.esa.int/web/gaia/dpac/consortium). Funding for the DPAC has been provided by national institutions, in particular the institutions participating in the Gaia Multilateral Agreement. This work is based, in part, on observations obtained with the Hobby–Eberly Telescope (HET), which is a joint project of the University of Texas at Austin, the Pennsylvania State University, Ludwig-Maximillians-Universitaet Muenchen, and Georg-August Universitaet Goettingen. The HET is named in honour of its principal benefactors, W. P. Hobby and R. E. Eberly. The Low Resolution Spectrograph 2 (LRS2) was developed and funded by the University of Texas at Austin McDonald Observatory and Department of Astronomy, and by Pennsylvania State University. We thank the Leibniz-Institut für Astrophysik Potsdam (AIP) and the Institut fur Astrophysik Goettingen (IAG) for their contributions to the construction of the integral field units. I.d.R. acknowledges support through the project CORTEX (project number NWA.1160.18.316) of the research programme NWA-ORC, which is (partly) financed by the Dutch Research Council (NWO). Parts of this research were conducted by the Australian Research Council Centre of Excellence for Gravitational Wave Discovery (OzGrav), project number CE230100016. K.M.R. acknowledges funding from the Vici research project ARGO (project number 639.043.815). Parts of this research were conducted by the Australian Research Council Centre of Excellence for Gravitational Wave Discovery (OzGrav), project number CE170100004. A.R. acknowledges funding from the NWO Aspasia grant (grant number 015.016.033). J.W.T.H. and the AstroFlash research group at McGill University, University of Amsterdam, ASTRON, and JIVE are supported by a Canada Excellence Research Chair in Transient Astrophysics (grant number CERC-2022-00009); the European Research Council (ERC) under the European Union's Horizon 2020 research and innovation programme ('EuroFlash'; grant agreement number 101098079); and an NWO-Vici grant ('AstroFlash'; grant number VI.C.192.045). Basic research in radio astronomy at the US Naval Research Laboratory is supported by 6.1 Base Funding. Construction and installation of VLITE was supported by the NRL Sustainment Restoration and Maintenance fund. S.M. and G.S. acknowledge funding from NASA XRP Grant 80NSSC24K0155.

Author contributions

I.d.R. performed the transient search on LoTSS data and led the writing of the Article with suggestions from all co-authors. I.d.R. is the principal investigator of the LOFAR follow-up observations and performed the analysis of the radio data and optical spectra. K.M.R. did the periodicity search and undertook the timing and DM analysis. C.G.B. developed the methods to fit the broadband photometry. A.R., R.A.M.J.W. and T.W.S. contributed to the development of the transient pipeline. A.R., R.A.M.J.W. and J.W.T.H. helped steer the project and plan follow-up observations. C.G.B., K.M.R. and S.t.V. commissioned the simultaneous beamformed and interferometric observations for the LOFAR follow-up proposal. C.D.K. performed the MMT spectroscopic observations. G.S. and S.M. acquired the HET LRS2 data, and G.Z. performed the reductions. J.R.C. contributed to the analysis of the spectral data and writing of the sections on stellar activity. G.S. analysed the ZTF data. W.P. and T.E.C. led the search through archival VLITE data. R.A.D.W. performed the analysis of the UVOT data. V.M. allowed the use of the periodicity search code ALTRIS.

Funding

Open access funding provided by the University of Sydney.

Competing interests

The authors declare no competing interests.

Additional information

Extended data is available for this paper at https://doi.org/10.1038/s41550-025-02491-0.

Supplementary information The online version contains supplementary material available at https://doi.org/10.1038/s41550-025-02491-0.

Correspondence and requests for materials should be addressed to I. de Ruiter.

Peer review information *Nature Astronomy* thanks Bradley Meyers and Ingrid Pelisoli for their contribution to the peer review of this work.

Reprints and permissions information is available at www.nature.com/reprints.

Publisher's note Springer Nature remains neutral with regard to jurisdictional claims in published maps and institutional affiliations.

Open Access This article is licensed under a Creative Commons Attribution 4.0 International License, which permits use, sharing, adaptation, distribution and reproduction in any medium or format, as long as you give appropriate credit to the original author(s) and the source, provide a link to the Creative Commons licence, and indicate if changes were made. The images or other third party material in this article are included in the article's Creative Commons licence, unless indicated otherwise in a credit line to the material. If material is not included in the article's Creative Commons licence and your intended use is not permitted by statutory regulation or exceeds the permitted use, you will need to obtain permission directly from the copyright holder. To view a copy of this licence, visit http://creativecommons.org/licenses/by/4.0/.

© Crown 2025, corrected publication 2025

[1]Sydney Institute for Astronomy, School of Physics, The University of Sydney, Sydney, New South Wales, Australia. [2]Anton Pannekoek Institute for Astronomy, University of Amsterdam, Amsterdam, the Netherlands. [3]ARC Centre of Excellence for Gravitational Wave Discovery (OzGrav), Hawthorn, Victoria, Australia. [4]Astrophysics, University of Oxford, Oxford, UK. [5]ASTRON, Netherlands Institute for Radio Astronomy, Dwingeloo, the Netherlands. [6]Center for Interdisciplinary Exploration and Research in Astrophysics, Northwestern University, Evanston, IL, USA. [7]Leiden Observatory, Leiden University, Leiden, the Netherlands. [8]Trottier Space Institute, McGill University, Montreal, Quebec, Canada. [9]Department of Physics, McGill University, Montreal, Quebec, Canada. [10]US Naval Research Laboratory, Remote Sensing Division, Washington, DC, USA. [11]SKA Observatory, Jodrell Bank, Macclesfield, UK. [12]Hobby Eberly Telescope, University of Texas, Austin, Austin, TX, USA. [13]Department of Astronomy and Astrophysics, Penn State University, University Park, PA, USA. [14]Center for Exoplanets and Habitable Worlds, Penn State University, University Park, PA, USA. ✉e-mail: iris.deruiter@sydney.edu.au

https://doi.org/10.1038/s41550-025-02491-0

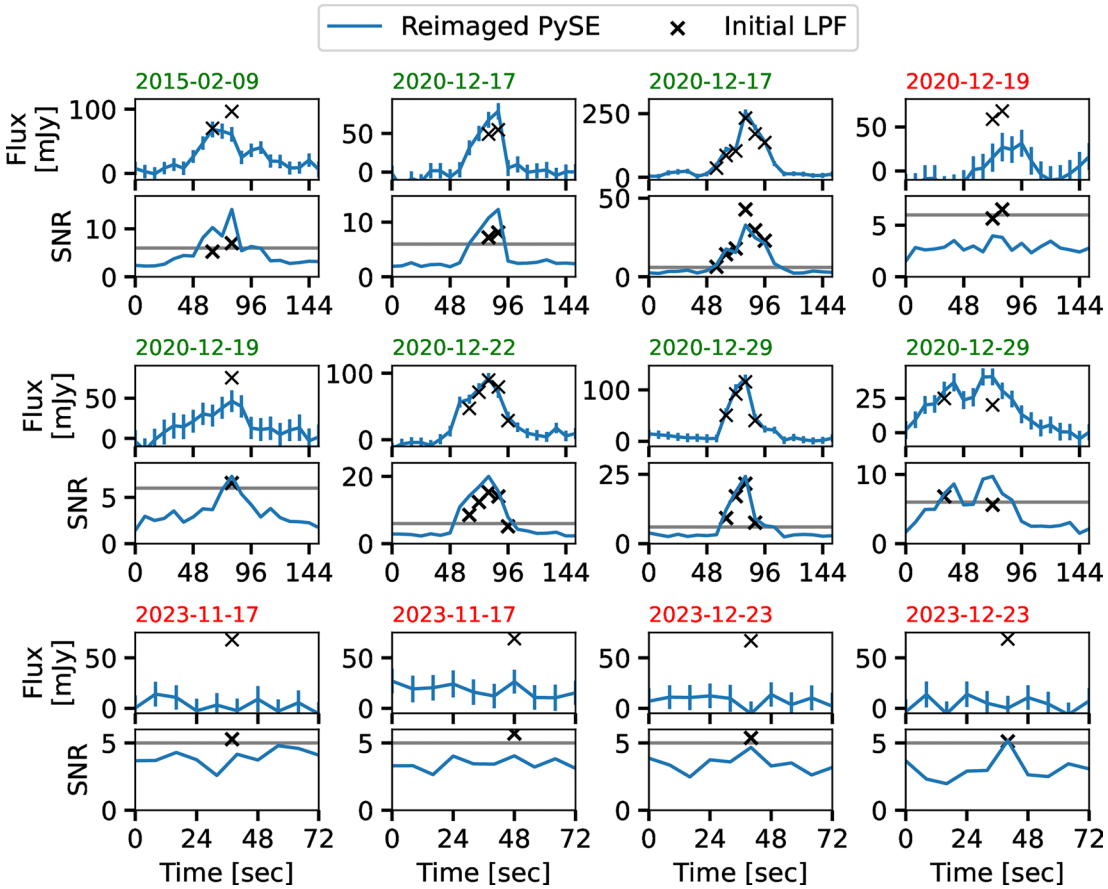

Extended Data Fig. 1 | Gallery of ILT J1101+5521 pulse profiles. For each pulse both the light curve and the SNR as a function of time are shown. The error bars on the flux indicate 1σ errors. The crosses indicate the initial values for the flux and SNR that triggered the detection of this pulse. These detections are done with a quick source finder (LPF) on lower-quality (but 'quick') images. The blue light curves indicate the full pulse profile determined with a sophisticated source finder (PYSE) using images that are of higher quality. The horizontal grey lines indicate the signal-to-noise ratio threshold used in the search with the 'quick' images.

https://doi.org/10.1038/s41550-025-02491-0

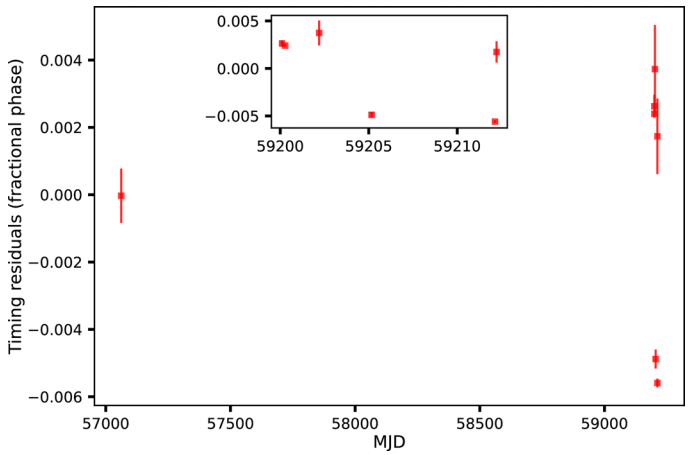

Extended Data Fig. 2 | Timing residuals divided by the period as a function of MJD. The timing residual is defined as the difference between the measured time of arrival (ToA) and the ToA predicted by the timing model. The inset shows a zoomed in view of the last 6 ToAs. The error bars on the points indicate 1σ errors.

https://doi.org/10.1038/s41550-025-02491-0

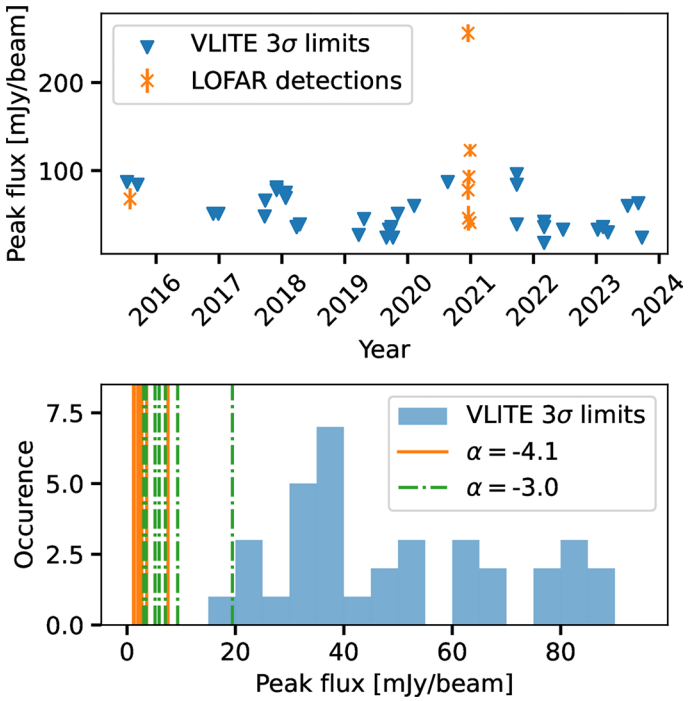

Extended Data Fig. 3 | Search for pulses from ILT J1101+5521 in archival VLITE data. Top panel: 3σ upper limits from VLITE 1-minute snapshot images (blue triangles) and the peak flux densities of the LOFAR detections (orange crosses) with 1σ error bars as a function of time. Bottom panel: distribution of 3σ upper limits from VLITE 1-minute snapshot images (blue) and the extrapolated LOFAR peak flux densities at 340 MHz (VLITE frequency) for a spectral index of $\alpha = -4.1$ (orange lines) and $\alpha = -3.0$ (green dashed dotted lines).

https://doi.org/10.1038/s41550-025-02491-0

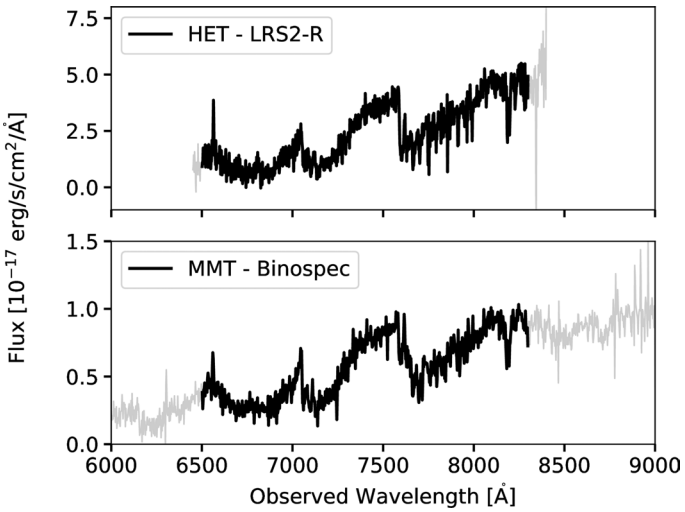

Extended Data Fig. 4 | Spectrum of the M dwarf associated with ILT J1101+5521. The top panel shows the LRS2-R spectra obtained with the HET. The bottom panel shows a coadded spectrum of the 6 epochs obtained by the Binospec instrument on the MMT. The highlighted parts of the spectrum are used for radial velocity fitting. Both spectra have been binned by a factor of two to increase signal-to-noise.

https://doi.org/10.1038/s41550-025-02491-0

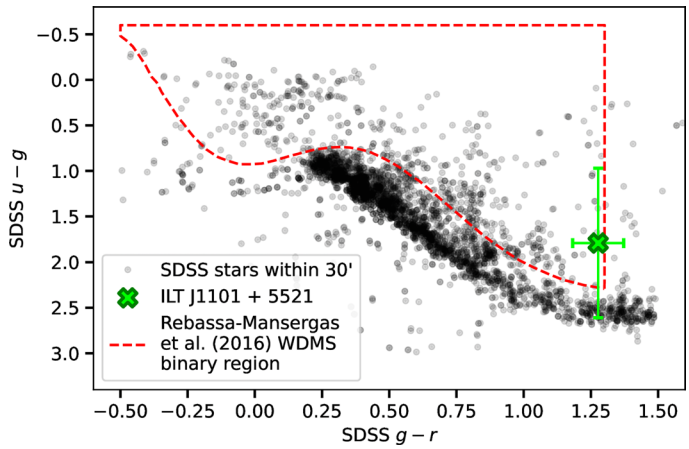

Extended Data Fig. 5 | Colour-colour diagram of ILT J1101+5521 compared to a sample of nearby stars and selection criteria for white dwarf binaries. SDSS objects classified as stars with colour uncertainties < 0.1 mag and within 30′ of ILT J1101+5521. The red dashed line shows the colour-colour selection of white dwarf - M dwarf binaries from[7]. The green data point shows ILT J1101+5521 including colour uncertainties.

https://doi.org/10.1038/s41550-025-02491-0

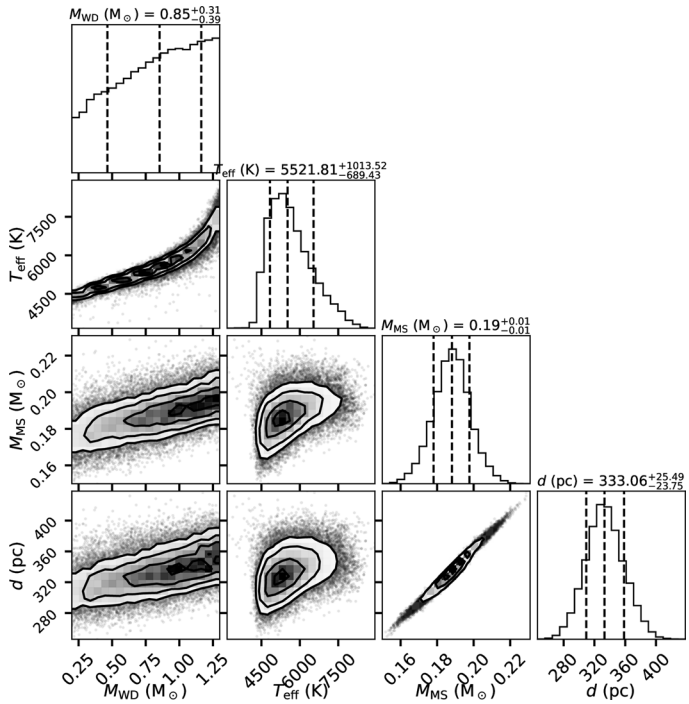

Extended Data Fig. 6 | One and two-dimensional projections of the posterior probability distributions of the parameters used to fit the broadband photometry data of ILT J1101+5521. The broadband photometry fits are presented in Fig. 3. This Figure was created using[109].

https://doi.org/10.1038/s41550-025-02491-0

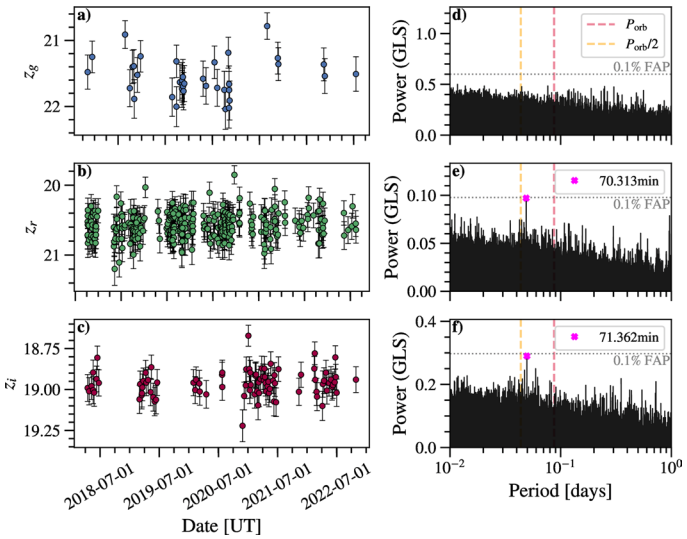

Extended Data Fig. 7 | ZTF photometry of ILT J1101+5521. Data are shown for three filters: **(a)** z_g, **(b)** z_r, and **(c)** z_i. Error bars denote 1σ uncertainties. **(d-f)** Generalized Lomb-Scargle periodograms for each filter. The red vertical line denotes the P_{orb} = 125.52 min orbital period of the system, and the orange vertical line denotes half the orbital period ($P_{orb}/2$) expected from ellipsoidal variations. There are no peaks above the 0.1% false alarm probability threshold (grey horizontal dotted lines) at the orbital period or half the orbital period. In the z_r and z_i filters the maximum peaks correspond to periods of 70.3 min and 71.4 min, but are below the 0.1% false alarm probability line. The power in the periodogram is normalized following [110].

https://doi.org/10.1038/s41550-025-02491-0

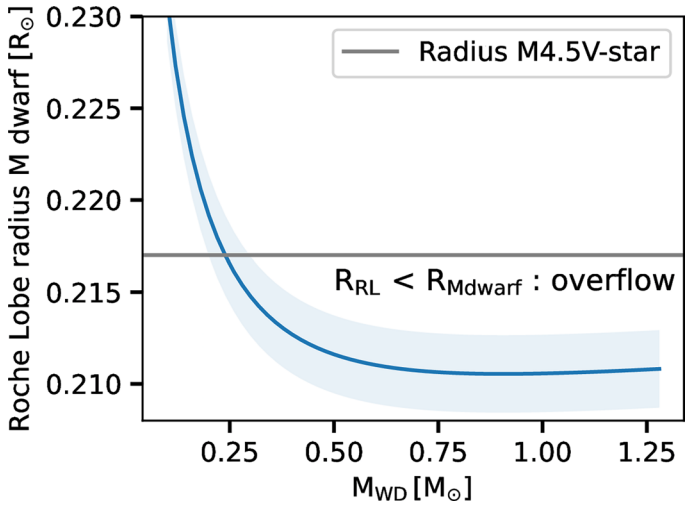

Extended Data Fig. 8 | The M dwarf Roche-Lobe radius as a function of white dwarf mass. The Roche-Lobe radius is calculated using the Eggleton approximation[111], the blue band indicates the 1% error on the mean of the Eggleton approximation. Here we assume an M dwarf mass of $0.188 M_{\odot}$ (determined from broadband photometry), and an M4.5V dwarf radius of $0.217 R_{\odot}$.

https://doi.org/10.1038/s41550-025-02491-0

Extended Data Table 1 | LOFAR observations of ILT J1101+5521

Observation ID	Start time UT, J2000	Duration [sec]	Peak flux density [mJy/beam]
L259781	2015-02-08 20:11:00	31199	68 ± 12
L801324	2020-12-17 01:12:00	28799	78 ± 11 , 256 ± 10*
L801338	2020-12-19 00:28:42	28799	46 ± 14
L801366	2020-12-21 23:41:00	28799	93 ± 8
L801380	2020-12-28 23:47:14	28799	123 ± 7, 41 ± 6
L2030101	2023-11-17 04:20:00	14400	-
L2031002	2023-11-24 03:22:00	14400	-
L2031009	2023-12-03 04:00:00	14400	-
L2031018	2023-12-23 03:30:00	14400	-

The final column shows the individual pulse peak flux entities for observations with one or more detections, whereas '-' indicates observations without detections. *: Peak flux density from the 1-second time slices is 431 mJy/beam.